

The Cosmic Microwave Background for Pedestrians: A Review for Particle and Nuclear Physicists

Dorothea Samtleben¹⁾ Suzanne Staggs²⁾ Bruce Winstein³⁾

1) Max-Planck-Institut für Radioastronomie, Bonn 2) Princeton University

3) The University of Chicago

Contents

1	INTRODUCTION	2
1.1	The Standard Paradigm	2
1.2	Fundamental Physics in the CMB	3
1.3	History	4
1.4	Introduction to the Angular Power Spectrum	6
1.5	Current Understanding of the Temperature Field	7
1.6	Acoustic Oscillations	7
1.7	How Spatial Modes Look Like Angular Anisotropies	8
1.8	CMB Polarization	9
1.9	Processes after Decoupling: Secondary Anisotropies	11
1.10	What We Learn from the CMB Power Spectrum	13
1.11	Discussion of Cosmological Parameters	15
2	FOREGROUNDS	17
2.1	Overview	17
2.2	Foreground Removal	20
3	METHODS OF DETECTION	20
3.1	The CMB Experiment Basics	21
3.2	The Detection Techniques	21
3.3	Observing Strategies	26
3.4	Techniques of Data Analysis	28
4	FUTURE PROSPECTS	30
4.1	The Next Satellite Experiment	31
5	CONCLUDING REMARKS	32
6	ACKNOWLEDGMENTS	33

Abstract

We intend to show how fundamental science is drawn from the patterns in the temperature and polarization fields of the cosmic microwave background (CMB) radiation, and thus to motivate the field of CMB research. We discuss the field's history, potential science and current status, contaminating foregrounds, detection and analysis techniques and future prospects. Throughout the review we draw comparisons to particle physics, a field that has many of the same goals and that has gone through many of the same stages.

1 INTRODUCTION

What is all the fuss about noise? In this review we endeavor to convey the excitement and promise of studies of the cosmic microwave background (CMB) radiation to scientists not engaged in these studies, particularly to particle and nuclear physicists. Although the techniques for both detection and data processing are quite far apart from those familiar to our intended audience, the science goals are aligned. We do not emphasize mathematical rigor¹, but rather attempt to provide insight into (a) the processes that allow extraction of fundamental physics from the observed radiation patterns and (b) some of the most fruitful methods of detection.

In Section 1, we begin with a broad outline of the most relevant physics that can be addressed with the CMB and its polarization. We then treat the early history of the field, how the CMB and its polarization are described, the physics behind the acoustic peaks, and the cosmological physics that comes from CMB studies. Section 2 presents the important foreground problem: primarily galactic sources of microwave radiation. The third section treats detection techniques used to study these extremely faint signals. The promise (and challenges) of future studies is presented in the last two sections. In keeping with our purposes, we do not cite an exhaustive list of the ever expanding literature on the subject, but rather indicate several particularly pedagogical works.

1.1 The Standard Paradigm

Here we briefly review the now standard framework in which cosmologists work and for which there is abundant evidence. We recommend readers to the excellent book *Modern Cosmology* by Dodelson (2). Early in its history (picoseconds after the Big Bang), the energy density of the Universe was divided among matter, radiation, and dark energy. The matter sector consisted of all known elementary particles and included a dominant component of dark matter, stable particles with negligible electromagnetic interactions. Photons and neutrinos (together with the kinetic energies of particles) comprised the radiation energy density, and the dark energy component some sort of fluid with a negative pressure appears to have had no importance in the early Universe, although it is responsible for its acceleration today.

Matter and radiation were in thermal equilibrium, and their combined energy density drove the expansion of space, as described by general relativity. As the Universe expanded, wavelengths were stretched so that particle energies (and hence the temperature of the Universe) decreased: $T(z) = T(0)(1 + z)$, where z is the redshift and $T(0)$ is the temperature at $z = 0$, or today. There were slight overdensities in the initial conditions that, throughout the expansion, grew through gravitational instability, eventually forming the structure we observe in today's Universe: myriad stars, galaxies, and clusters of galaxies.

The Universe was initially radiation dominated. Most of its energy density was in photons, neutrinos, and kinetic motion. After the Universe cooled to the point at which the energy in rest mass equaled that in kinetic motion (matter-radiation equality), the expansion rate slowed and the Universe became matter dominated, with most of its energy tied up in the masses of slowly moving, relatively heavy stable particles: the proton and deuteron from the baryon sector and the dark matter particle(s). The next important era is termed either decoupling, recombination, or last scattering. When the temperature reached roughly 1 eV, atoms (mostly H) formed and the radiation cooled too much to ionize. The Universe became transparent, and it was during this era that the CMB we see today was emitted, when physical separations were 1000 times smaller than today ($z \approx 1000$). At this point, less than one million years into the expansion, when electro-

¹This review complements the one by Kamionkowski and Kosowsky (1).

magnetic radiation ceased playing an important dynamical role, baryonic matter began to collapse and cool, eventually forming the first stars and galaxies. Later, the first generation of stars and possibly supernova explosions seem to have provided enough radiation to completely reionize the Universe (at $z \approx 10$). Throughout these stages, the expansion was decelerated by the gravitational force on the expanding matter. Now we are in an era of cosmic acceleration ($z \leq 2$), where we find that approximately 70% of the energy density is in the fluid that causes the acceleration, 25% is in dark matter, and just 5% is in baryons, with a negligible amount in radiation.

1.2 Fundamental Physics in the CMB

The CMB is a record of the state of the Universe at a fraction of a million years after the Big Bang, after a quite turbulent beginning, so it is not immediately obvious that any important information survives. Certainly the fundamental information available in the collisions of elementary particles is best unraveled by observations within nanoseconds of the collision. Yet even in this remnant radiation lies the imprint of fundamental features of the Universe at its earliest moments.

1.2.1 CMB features: evidence for inflation.

One of the most important features of the CMB is its Planck spectrum. It follows the blackbody curve to extremely high precision, over a factor of approximately 1000 in frequency (see Figure 1). This implies that the Universe was in thermal equilibrium when the radiation was released (actually long before, as we see below), which was at a temperature of approximately 3000 K. Today it is near 3 K.

An even more important feature is that, to better than a part in 10^4 , this temperature is the same over the entire sky. This is surprising because it strongly implies that everything in the observable Universe was in thermal equilibrium at one time in its evolution. Yet at any time and place in the expansion history of the Universe, there is a causal horizon defined by the distance light (or gravity) has traveled since the Big Bang; at the decoupling era, this horizon corresponded to an angular scale of approximately 1° , as observed today. The uniformity of the CMB on scales well above 1° is termed the horizon problem.

The most important feature is that there are differences in the CMB temperature from place to place, at the level of 10^{-5} , and that these fluctuations have coherence beyond the horizon at the time of last scattering. The most viable notion put forth to address these observations is the inflationary paradigm, which postulates a very early period of extremely rapid expansion of the Universe. Its scale factor increased by approximately 21 orders of magnitude in only approximately 10^{35} s. Before inflation, the small patch that evolves into our observable Universe was likely no larger across than the Planck length, its contents in causal contact and local thermodynamic equilibrium. The process of superluminal inflation disconnects regions formally in causal contact. When the expansion slowed, these regions came back into the horizon and their initial coherence became manifest.

The expansion turns quantum fluctuations into (nearly) scale-invariant CMB inhomogeneities, meaning that the fluctuation power is nearly the same for all threedimensional Fourier modes. So far, observations agree with the paradigm, and scientists in the field use it to organize all the measurements. Nevertheless, we are far from understanding the microphysics driving inflation. The number of models and their associated parameter spaces greatly exceed the number of relevant observables. New observations, particularly of the CMB polarization, promise a more direct look at inflationary physics, moving our understanding from essentially kinematical to dynamical.

1.2.2 Probing the Universe when $T = 10^{16}$ GeV.

For particle physicists, probing microphysics at energy scales beyond accelerators using cosmological observations is attractive. The physics of inflation may be associated with the grand unification scale, and if so, there could be an observable signature in the CMB: gravity waves. Metric perturbations, or gravity waves (also termed tensor modes), would have been created during inflation, in addition to the density perturbations (scalar modes) that give rise to the structure in the Universe today.

In the simplest of inflationary models, there is a direct relation between the energy scale of inflation and the strength of these gravity waves. The notion is that the Universe initially had all its energy in a scalar field Φ displaced from the minimum of its potential V . $V(\Phi)$ is suitably constructed so that slowly rolls down its potential, beginning the inflationary era of the Universe, which terminates only when Φ approaches its minimum.

Inflation does not predict the level of the tensor (or even scalar) modes. The parameter $r = T/S$ is the tensor-to-scalar ratio for fluctuation power; it depends on the energy scale at which inflation began. Specifically, the initial height of the potential V_i depends on r , as $V_i = r(0.003M_{pl})^4$. A value of $r = 0.001$, perhaps the smallest detectable level, corresponds to $V_i^{0.25} = 6.5 \times 10^{15} GeV$.

The tensor modes leave distinct patterns on the polarization of the CMB, which may be detectable. This is now the most important target for future experiments. They also have effects on the temperature anisotropies, which currently limit r to less than approximately 0.3.

1.2.3 How neutrino masses affect the CMB.

It is a remarkable fact that even a slight neutrino mass affects the expansion of the Universe. When the dominant dark matter clusters, it provides the environment for baryonic matter to collapse, cool, and form galaxies. As described above, the growth of these structures becomes more rapid in the matter-dominated era. If a significant fraction of the dark matter were in the form of neutrinos with electron-volt-scale masses (nonrelativistic today), these would have been relativistic late enough in the expansion history that they could have moved away from overdense regions and suppressed structure growth. Such suppression alters the CMB patterns and provides some sensitivity to the sum of the neutrino masses. Note also that gravitational effects on the CMB in its passage from the epoch (or surface) of last scattering to the present leave signatures of that structure and give an additional (and potentially more sensitive) handle on the neutrino masses (see Section 1.9.2).

1.2.4 Dark energy.

We know from the CMB that the geometry of the Universe is consistent with being flat. That is, its density is consistent with the critical density. However, the overall density of matter and radiation discerned today (the latter from the CMB directly) falls short of accounting for the critical density by approximately a factor of three, with little uncertainty. Thus, the CMB provides indirect evidence for dark energy, corroborating supernova studies that indicate a new era of acceleration. Because the presence and possible evolution of a dark energy component alter the expansion history of the Universe, there is the promise of learning more about this mysterious component.

1.3 History

In 1965, Penzias and Wilson (3), in trying to understand a nasty noise source in their experiment to study galactic radio emission, discovered the CMB arguably the most im-

portant discovery in all the physical sciences in the twentieth century. Shortly thereafter, scientists showed that the radiation was not from radio galaxies or reemission of starlight as thermal radiation. This first measurement was made at a central wavelength of 7.35 cm, far from the blackbody peak. The reported temperature was $T = 3.5 \pm 1K$. However, for a blackbody, the absolute flux at any known frequency determines its temperature. Figure 1 shows the spectrum of detected radiation for different temperatures. There is a linear increase in the peak position and in the flux at low frequencies (the Rayleigh-Jeans part of the spectrum) as temperature increases.

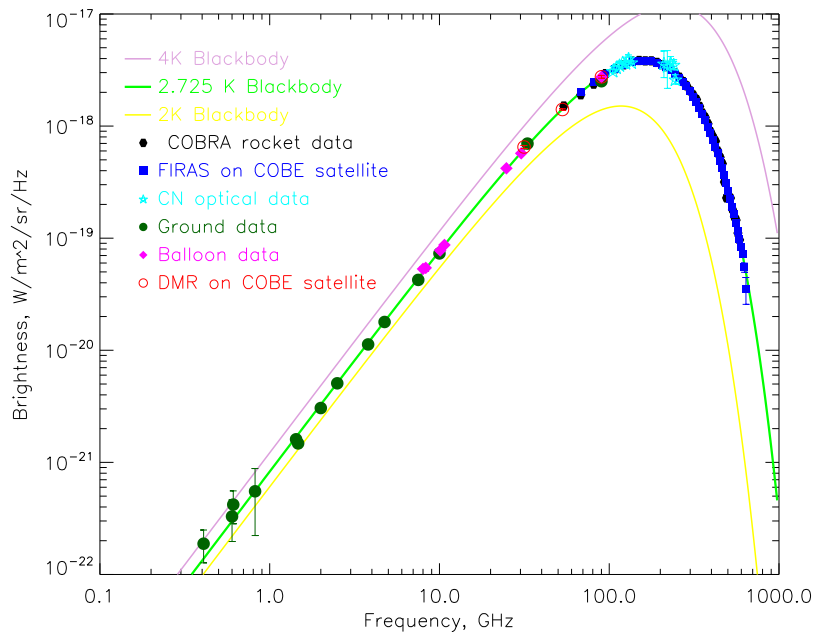


Figure 1: Measurements of the CMB flux vs. frequency together with a fit to the data. Superposed are the expected black body curves for $T = 2\text{ K}$ and $T = 40\text{ K}$.

Multiple efforts were soon mounted to confirm the blackbody nature of the CMB and to search for its anisotropies. Partridge (4) gives a very valuable account of the early history of the field. However, there were false observations, which was not surprising given the low ratio of signal to noise. Measurements of the absolute CMB temperature are at milli-Kelvin levels, whereas relative measurements between two places on the sky are at micro-Kelvin levels. By 1967, Partridge and Wilkinson had shown, over large regions of the sky, that $\Delta T/T \leq (1 - 3) \times 10^{-3}$, leading to the conclusion that the Universe was in thermal equilibrium at the time of decoupling (4). However, nonthermal injections of energy even at much earlier times, for example, from the decays of long-lived relic particles, would distort the spectrum. It is remarkable that current precise measurements of the blackbody spectrum can push back the time of significant injections of energy to when the Universe was barely a month old (5). Thus, recent models that attribute the dark matter to gravitinos as decay products of long-lived supersymmetric weakly interacting massive particles (SUSY WIMPs) (6) can only tolerate lifetimes of less than approximately one month.

The solar system moves with velocity $\beta \approx 3 \times 10^{-3}$, causing a dipole anisotropy of

a few milli-Kelvins, first detected in the 1980s. (Note that the direction of our motion was not the one initially hypothesized from motions of our local group of galaxies.) The first detection of primordial anisotropy came from the COBE satellite (7) in 1992, at the level of 10^{-5} (30 μK), on scales of approximately 10° and larger. The impact of this detection matched that of the initial discovery. It supported the idea that structure in the Universe came from gravitational instability to overdensities. The observed anisotropies are a combination of the original ones at the time of decoupling and the subsequent gravitational red- or blueshifting as photons leave over- or underdense regions.

1.4 Introduction to the Angular Power Spectrum

Here we describe the usual techniques for characterizing the temperature field. First, we define the normalized temperature Θ in direction $\hat{\mathbf{n}}$ on the celestial sphere by the deviation ΔT from the average: $\Theta(\hat{\mathbf{n}}) = \frac{\Delta T}{\langle T \rangle}$. Next, we consider the multipole decomposition of this temperature field in terms of spherical harmonics Y_{lm} :

$$\Theta_{lm} = \int \Theta(\hat{\mathbf{n}}) Y_{lm}^*(\hat{\mathbf{n}}) d\Omega, \quad (1)$$

where the integral is over the entire sphere.

If the sky temperature field arises from Gaussian random fluctuations, then the field is fully characterized by its power spectrum $\Theta_{lm}^* \Theta_{l'm'}$. The order m describes the angular orientation of a fluctuation mode, but the degree (or multipole) l describes its characteristic angular size. Thus, in a Universe with no preferred direction, we expect the power spectrum to be independent of m . Finally, we define the angular power spectrum C_l by $\langle \Theta_{lm}^* \Theta_{l'm'} \rangle = \delta_{ll'} \delta_{mm'} C_l$. Here the brackets denote an ensemble average over skies with the same cosmology. The best estimate of C_l is then from the average over m .

Because there are only the $(2l+1)$ modes with which to detect the power at multipole l , there is a fundamental limit in determining the power. This is known as the cosmic variance (just the variance on the variance from a finite number of samples):

$$\frac{\Delta C_l}{C_l} = \sqrt{\frac{2}{2l+1}}. \quad (2)$$

The full uncertainty in the power in a given multipole degrades from instrumental noise, finite beam resolution, and observing over a finite fraction of the full sky, as shown below in Equation 9.

For historical reasons, the quantity that is usually plotted, sometimes termed the TT (temperature-temperature correlation) spectrum, is

$$\Delta T^2 \equiv \frac{l(l+1)}{2\pi} C_l T_{CMB}^2, \quad (3)$$

where T_{CMB} is the blackbody temperature of the CMB. This is the variance (or power) per logarithmic interval in l and is expected to be (nearly) uniform in inflationary models (scale invariant) over much of the spectrum. This normalization is useful in calculating the contributions to the fluctuations in the temperature in a given pixel from a range of l values:

$$\Delta T^2 = \int_{l_{min}}^{l_{max}} \frac{(2l+1)}{4\pi} C_l T_{CMB}^2 dl \quad (4)$$

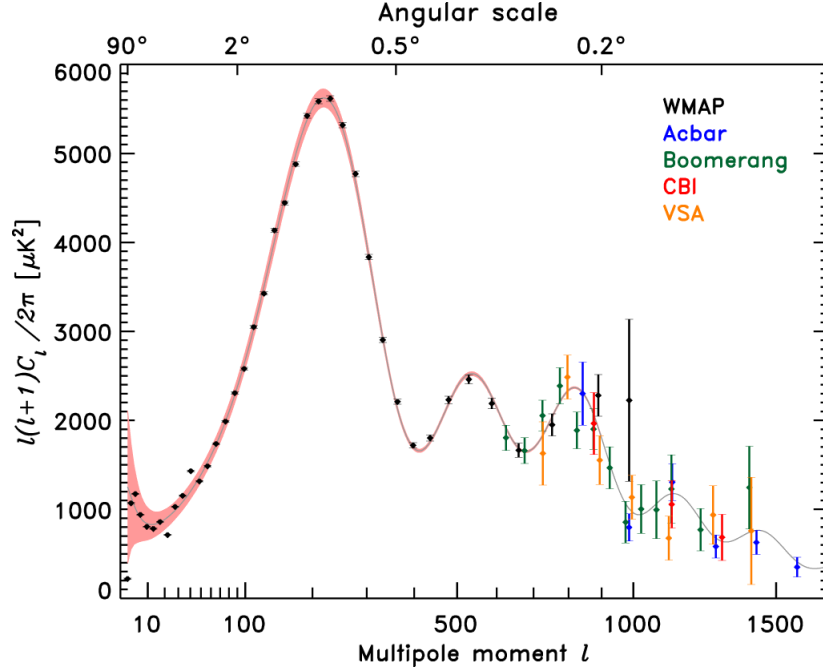


Figure 2: The TT Power Spectrum. Data from the Wilkinson Microwave Anisotropy Probe (WMAP) (8), and high- l data from other experiments are shown, in addition to the best-fit cosmological model to the WMAP data alone. Note the multipole scale on the bottom and the angular scale on the top. Figure courtesy of the WMAP science team

1.5 Current Understanding of the Temperature Field

Figure 2 shows the current understanding of the temperature power spectrum (from here-with we redefine C_l to have K^2 units by replacing C_l with $C_l T_{CMB}^2$). The region below $l \approx 20$ indicates the initial conditions. These modes correspond to Fourier modes at the time of decoupling, with wavelengths longer than the horizon scale. Note that were the sky describable by random white noise, the C_l spectrum would be flat and the TT power spectrum, defined by Equation 3, would have risen in this region like l^2 . The (pleasant) surprise was the observation of finite power at these superhorizon scales. At high l values, there are acoustic oscillations, which are damped at even higher l values. The positions and heights of the acoustic-oscillation peaks reveal fundamental properties about the geometry and composition of the Universe, as we discuss below.

1.6 Acoustic Oscillations

The CMB data reveal that the initial inhomogeneities in the Universe were small, with overdensities and underdensities in the dark matter, protons, electrons, neutrinos, and photons, each having the distribution that would arise from a small adiabatic compression or expansion of their admixture. An overdense region grows by attracting more mass, but only after the entire region is in causal contact.

We noted that the horizon at decoupling corresponds today to approximately 1° on the sky. Only regions smaller than this had time to compress before decoupling. For sufficiently small regions, enough time elapses that compression continues until the photon pressure is sufficient to halt the the electrons via Thomson scattering, and the protons follow the electrons to keep a charge balance. Inflation provides the initial conditions - zero velocity.

Decoupling preserves a snapshot of the state of the photon fluid at that time. Excellent pedagogical descriptions of the oscillations can be found at <http://background.uchicago.edu/~whu/>. Other useful pages are <http://wmap.gsfc.nasa.gov/>, <http://space.mit.edu/home/tegmark/index.html> and <http://www.astro.ucla.edu/~wright/intro.html>. Perturbations of particular sizes may have undergone (a) one compression, (b) one compression and one rarefaction, (c) one compression, one rarefaction, and one compression, and so on. Extrema in the density field result in maxima in the power spectrum.

Consider a standing wave permeating space with frequency ω and wave number k , where these are related by the velocity of displacements (the sound speed, $v_s \approx c/\sqrt{3}$) in the plasma: $\omega = kv_s$. The wave displacement A_k for this single mode can then be written as $A_k(x, t) \propto \sin(kx)\cos(\omega t)$. The displacement is maximal at time t_{dec} of decoupling for $k_{TT}v_s t_{dec} = \pi, 2\pi, 3\pi \dots$. We add the TT subscript to label these wave numbers associated with maximal autocorrelation in the temperature. Note that even in this tightly coupled regime, the Universe at decoupling was quite dilute, with a physical density of less than $10^{-20} g cm^{-3}$. Because the photons diffuse their mean free path is not infinitely short this pattern does not go on without bound. The overtones are damped, and in practice only five or six such peaks will be observed, as seen in Figure 2.

1.7 How Spatial Modes Look Like Angular Anisotropies

To help explain these ideas, we reproduce a few frames from an animation by W. Hu. Figure 3 shows a density fluctuation on the sky from a single k mode and how it appears to an observer at different times. The figure shows the particle horizon just after decoupling. This represents the farthest distance one could in principle see approximately the speed of light times the age of the Universe. An observer at the center of the gure could not by any means have knowledge of anything outside this region. Of course, just after decoupling, the observer could see a far shorter distance. Only then could light propagate freely.

The subsequent frames show how the particle horizon grows to encompass more corrugations of the original density fluctuation. At first the observer sees a dipole, later a quadrupole, then an octopole, and so on, until the present time when that single mode in density inhomogeneities creates very high multipoles in the temperature anisotropy.

It is instructive to think of how the temperature observed today at a spot on the sky arises from the local moments in the temperature field at the time of last scattering. It is only the lowest three moments that contribute to determining the anisotropies. The monopole terms are the ones transformed into the rich angular spectra. The dipole terms also have their contribution: The motion in the fluid oscillations results in Doppler shifts in the observed temperatures. Polarization, we see below, comes from local quadrupoles.

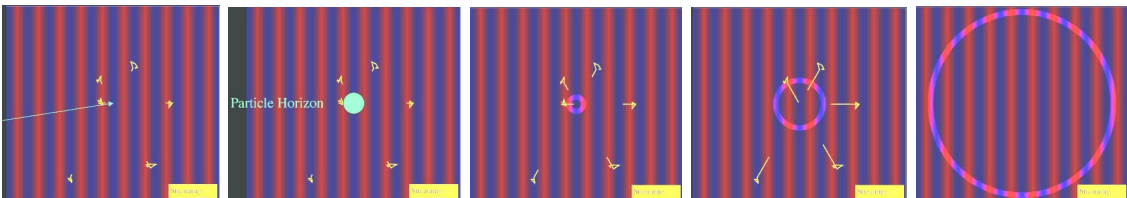


Figure 3: The Signature of one frozen mode after Decoupling.

These frames show one superhorizon temperature mode just after decoupling with representative photons last scattering and heading toward the observer at the center. Left to right: just after decoupling; the observer's particle horizon when only the temperature monopole can be detected; some time later when the quadrupole is detected; later still when the 12-pole is detected; and today, a very high, well aligned multipole, from just this single mode in k -space, is detected. Figure courtesy of W. Hu

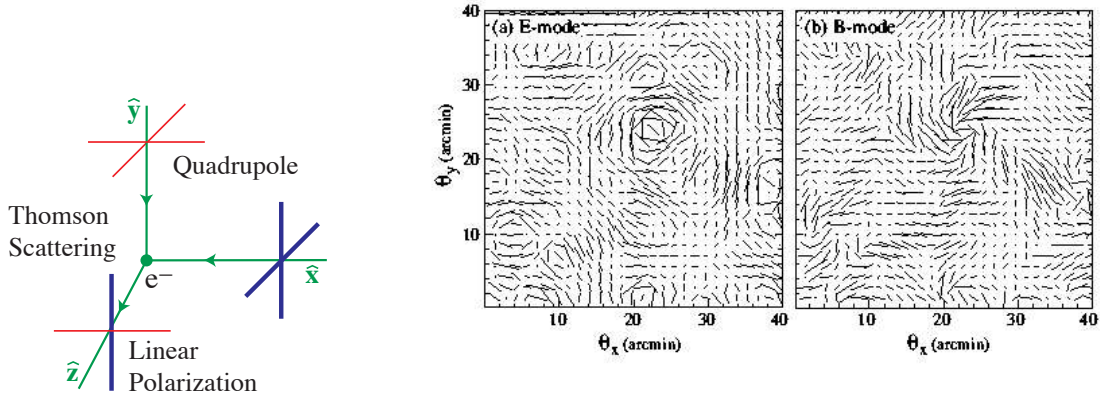


Figure 4: Generation of polarization. Left: Unpolarized but anisotropic radiation incident on an electron produces polarized radiation. Intensity is represented by line thickness. To an observer looking along the direction of the scattered photons (\hat{z}), the incoming quadrupole pattern produces linear polarization along the \hat{y} -direction. In terms of the Stokes parameters, this is $Q = (E_x^2 - E_y^2)/2$, the power difference detected along the \hat{x} - and \hat{y} -directions. Linear polarization needs one other parameter, corresponding to the power difference between 45° and 135° from the x-axis. This parameter is easily shown to be Stokes $U = E_x E_y$. Right: E and B polarization patterns. The length of the lines represents the degree of polarization, while their orientation gives the direction of maximum electric field. Frames courtesy of W. Hu.

1.7.1 Inflation revisited.

Inflation is a mechanism whereby fluctuations are created without violating causality. There does not seem to be a better explanation for the observed regularities. Nevertheless, Wolfgang Pauli's famous statement about the neutrino comes to mind: I have done a terrible thing: I have postulated a particle that cannot be detected!

Sometimes it seems that inflation is an idea that cannot be tested, or tested incisively. Of course Pauli's neutrino hypothesis did test positive, and similarly there is hope that the idea of inflation can reach the same footing. Still, we have not (yet) seen any scalar field in nature. We discuss what has been claimed as the smoking gun test of inflation the eventual detection of gravity waves in the CMB. However, will we ever know with certainty that the Universe grew in volume by a factor of 10^{63} in something like 10^{-35} s?

1.8 CMB Polarization

Experiments have now shown that the CMB is polarized, as expected. Researchers now think that the most fruitful avenue to fundamental physics from the CMB will be in precise studies of the patterns of the polarization. This section treats the mechanisms responsible for the generation of the polarization and how this polarization is described.

1.8.1 How polarization gets generated

If there is a quadrupole anisotropy in the temperature field around a scattering center, even if that radiation is unpolarized, the scattered radiation will be as shown in Figure 4: A linear polarization will be generated. The quadrupole is generated during decoupling, as shown in Figure 3. Because the polarization arises from scattering but said scattering dilutes the quadrupole, the polarization anisotropy is much weaker than that in the temperature field. Indeed with each scatter on the way to equilibrium, the polarization is

reduced. Any remaining polarization is a direct result of the cessation of scattering. For this reason, the polarization peaks at higher l values than does the temperature anisotropy. The local quadrupole on scales that are large in comparison to the mean free path is diluted from multiple scattering.

1.8.2 The E and B polarization fields.

The polarization field is both more complicated and richer than the temperature field. At each point in the sky, one must specify both the degree of polarization and the preferred direction of the electric field. This is a tensor field that can be decomposed into two types, termed E and B, which are, respectively, scalar and pseudoscalar fields, with associated power spectra. Examples of these polarization fields are depicted schematically in Figure 4. The E and B fields are more fundamental than the polarization field on the sky, whose description is coordinate-system dependent. In addition, E modes arise from the density perturbations (which do not produce B modes) that we describe, whereas the B modes come from the tensor distortions to the space-time metric (which do have a handedness). We mention here that the E and B fields are nonlocal. Their extraction from measurements of polarization over a set of pixels, often in a finite patch of sky, is a well-developed but subtle procedure (see Section 3.3).

The peaks in the EE (E-polarization correlated with itself) spectrum should be 180 out of phase with those for temperature: Polarization results from scattering and thus is maximal when the fluid velocity is maximal. Calculating the fluid velocity for the mode in Section 1.6, we find $k_{EE}v_s t_{dec} = \pi/2, 3\pi/2, 5\pi/2\dots$, defining modes with maximal EE power. The TE (E-polarization correlated with the temperature field) spectrum how modes in temperature correlate with those with E polarization is also of cosmological interest, with its own peak structure. Here we are looking at modes that have a maximum at decoupling in the product of their temperature and E-mode polarization (or velocity). Similarly, the appropriate maxima (which in this case can be positive or negative) are obtained when $k_{TE}v_s t_{dec} = \pi/4, 3\pi/4, 5\pi/4\dots$. Thus, between every peak in the TT power spectrum there should be one in the EE, and between every TT and EE pair of peaks there should be one in the TE.

1.8.3 Current understanding of polarization data

Figure 5 shows the EE results in addition to the expected power spectra in the standard cosmological model. Measurements of the TE cross correlation are also shown. The pattern of peaks in both power spectra is consistent with what was expected. What was unexpected was the enhancement at the lowest l values in the EE power spectrum. This is discussed in the next section.

The experiments reported in Figure 5, with 20 or fewer detectors, use a variety of techniques and operate in different frequency ranges. This is important in dealing with astrophysical foregrounds (see Section 2) that have a different frequency dependence from that of the CMB. Limits from current experiments on the B-mode power are now at the level of 1-10 μK^2 , far from the expected signal levels shown in Figure 6. The peak in the power spectrum (for the gravity waves) is at $l \approx 100$, the horizon scale at decoupling. The reader may wonder why the B modes fall off steeply above this scale and show no acoustic oscillations. The reason is simple: A tensor mode will give, for example, a compression in the x-direction followed by a rarefaction in the y-direction, but will not produce a net overdensity that would subsequently contract. In the final section we discuss experiments with far greater numbers of detectors aimed specifically at B-mode science. Note that such gravity waves have frequencies today of order 10^{-16} Hz. However, if their spectrum approximates one of scale invariance, they would in principle be detectable at frequencies

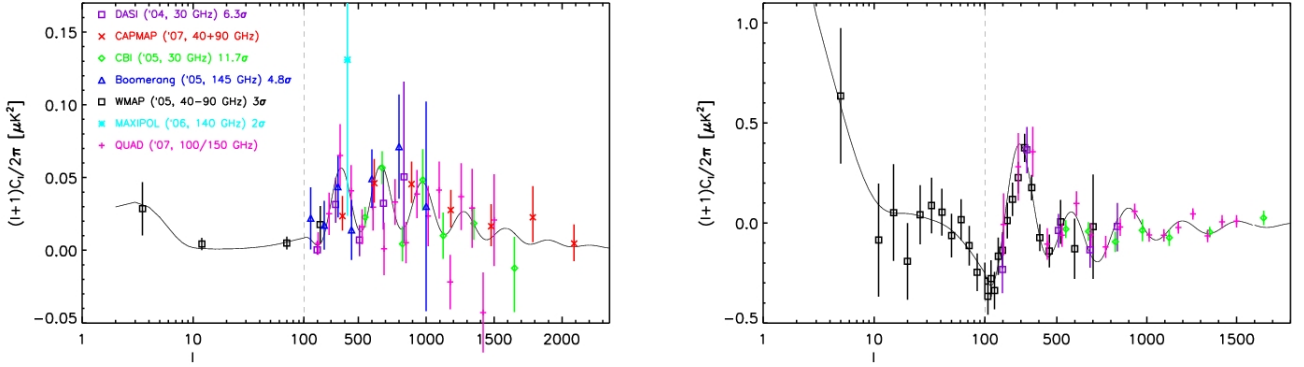


Figure 5: Measurements of EE (left) and TE (right) power spectra together with the WMAP best-fit cosmological model. The names of the experiments, their years of publication, and the frequency ranges covered are indicated, as well as the number of standard deviations with which each experiment claims a detection. Note the change from logarithmic to linear multipole scale at $l = 100$ and that to display features in the very low l range, we plot $(l + 1)C_l/2\pi$.

nearer 1 Hz, such as in the LISA experiment. This is discussed more fully in Reference 10.

1.9 Processes after Decoupling: Secondary Anisotropies

In this section we briefly discuss three important processes after decoupling: rescattering of the CMB in the reionized plasma of the Universe, lensing of the CMB through gravitational interactions with matter, and scattering of the CMB from hot gas in Galaxy clusters. Although these can be considered foregrounds perturbing the primordial information, each can potentially provide fundamental information.

1.9.1 Reionization.

The enhancement in the EE power spectrum at the very lowest l values in Figure 5 is the signature that the Universe was reionized after decoupling. This is a subject rich in astrophysics, but for our purposes it is important in that it provides another source for scattering and hence detection of polarization. From the Wilkinson Microwave Anisotropy Probe (WMAP) polarization data (11), one can infer an optical depth of order 10%, the fraction of photons scattering in the reionized plasma somewhere in the region of $z = 10$. This new scattering source can be used to detect the primordial gravity waves. The signature will show up at very low l values, corresponding to the horizon scale at reionization. Figure 6 shows that the region $l = 4 - 8$ should have substantial effects from gravity waves. Most likely, the only means of detecting such a signal is from space, and even from there it will be very difficult.

The polarization anisotropies for this very low l region are comparable to what is expected from the surface of last scattering ($l \approx 100$). There are disadvantages to each signature. At the lowest l values, galactic foregrounds are more severe, there are fewer modes in which to make a detection, and systematic errors are likely greater. At the higher values, there is a foreground that arises from E modes turning into B modes through gravitational lensing (the topic of the next section). Clearly, it will be important to detect the two signatures with the right relative strengths at these two very different scales.

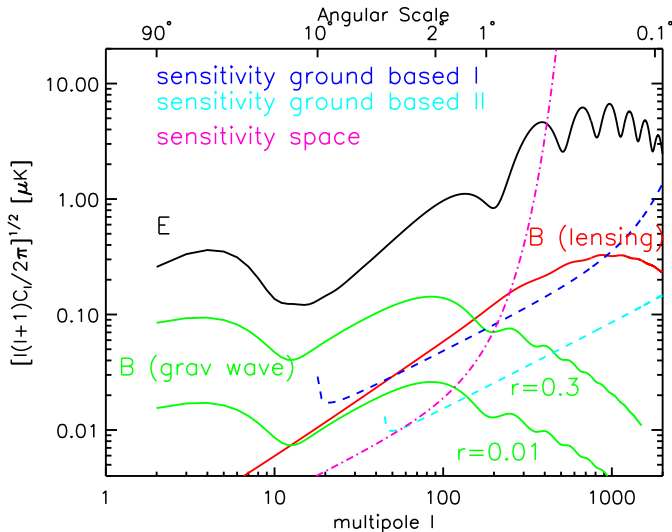


Figure 6: CMB polarization power spectra and estimated sensitivity of future experiments. The solid curves show the predictions for the E- and B-mode power spectra. The primordial B-mode power spectrum is shown for $r = 0.3$ and $r = 0.01$. The predicted B-mode signal power spectrum due to the distortion of E modes by weak gravitational lensing is also shown. Estimated statistical sensitivities for a new space mission (pink line) and two sample ground-based experiments, as considered in Reference 9, each with 1000 detectors operating for one year with 100% duty cycle (dark and light blue lines), are shown. Experiment I observes 4% of the sky, with a 6-arcmin resolution; experiment II observes 0.4% of the sky, with a 1-arcmin resolution.

1.9.2 Lensing of the CMB.

Both the temperature and polarization fields will be slightly distorted (lensed) when passing collapsing structures in the late Universe. The bending of light means that one is not looking (on the last scattering surface) where one thinks. Although lensing will affect both the polarization and T fields, its largest effect is on the B field, where it shifts power from E to B. Gravitational distortions, although preserving brightness, do not preserve the E and B nature of the polarization patterns.

Figure 6 also shows the expected power spectrum of these lensed B modes. Because this power is sourced by the E modes, it roughly follows their shape, but with ΔT suppressed by a factor of 20. The peak structure in the E modes is smoothed, as the structures doing the lensing are degree scale themselves. Owing to the coherence of the lensing potential for these modes, there is more information than just the power spectrum, and work is ongoing to characterize the expected cross correlation between different multipole bands. This signal should be detectable in next-generation polarization experiments. For our purposes, the most interesting aspect of this lensing is the handle it can potentially give on the masses of the neutrinos, as more massive neutrinos limit the collapse of matter along the CMB trajectories. All other parameters held fixed, there is roughly a factor-of-two change in the magnitude of the B signal for a 1-eV change in the mean neutrino mass.

1.9.3 CMB scattering since reionization.

At very small angular scales – l values of a few thousand, way beyond where the acoustic oscillations are damped – there are additional effects on the power spectra that result from the scattering of CMB photons from electrons after the epoch of reionization, including scattering from gas heated from falling deep in the potential wells of Galaxy clusters (the Sunyaev- Zel’dovich, or SZ, effect). These nonlinear effects are important as they can help in untangling (a) when the first structures formed and (b) the role of dark energy.

1.10 What We Learn from the CMB Power Spectrum

In this section, we show how the power spectrum information is used to determine important aspects of the Universe. This is normally known as parameter estimation, where the parameters are those that define our cosmology. The observable power spectrum is a function of at least 11 such basic parameters. As we discuss below, some are better constrained than others.

First, there are four parameters that characterize the primordial scalar and tensor fluctuation spectra before the acoustic oscillations, each of which is assumed to follow a power law in wave number. These four are the normalization of the scalar fluctuations (A_s), the ratio of tensor to scalar fluctuations r , and the spectral indices for both (historically denoted with $n_s - 1$ and n_t). Second, there is one equation-of-state parameter (w) that is the ratio of the pressure of the dark energy to its energy density, and one parameter that gives the optical depth (τ) from the epoch of reionization. Finally, there are five parameters that characterize the present Universe: its rate of expansion (Hubble constant, with $H_0 = h \cdot 100 \text{ km s}^{-1} \text{ Mpc}^{-1}$), its curvature (Ω_k), and its composition (baryon density, matter density, and dark energy density). The latter three are described in terms of energy densities with respect to the critical density normalized to the present epoch: $\omega_b = \Omega_b h^2$, $\omega_m = \Omega_m h^2$, and $\omega_\Lambda = \Omega_\Lambda h^2$. Just 10 of these are independent as $\Omega_m + \Omega_\Lambda + \Omega_k = 1$.

Even though the CMB data set itself consists of hundreds of measurements, they are not sufficiently orthogonal with respect to the 10 independent parameters for each to be determined independently; there are significant degeneracies. Hence, it is necessary to make assumptions that constrain the values of those parameters upon which the data have little leverage. In some cases, such prior assumptions (priors) can have large effects on the other parameters, and there is as yet no standard means of reporting results.

Several teams have done analyses [WMAP (11, 12), CBI (13), Boomerang (14), see also Reference 15]. Here we first discuss the leverage that the CMB power spectra have on the cosmological parameters. Then we give a flavor for the analyses, together with representative results. We consider analyses, done by the several teams, with just the six most important parameters: $\omega_b, \omega_m, A_s, n_s, \tau$, and h , where the other five are held fixed. For this discussion we are guided by Reference 12.

Completely within CMB data, there is a geometrical degeneracy between Ω_k , a contribution to the energy density from the curvature of space, and Ω_m . However, taking a very weak prior of $h > 0.5$, the WMAP team, using just their first-year data, determined that $\Omega_k = 0.03 \pm 0.03$, that is, no evidence for curvature. We assume $\Omega_k = 0$ unless otherwise noted. This conclusion has gotten stronger with the three-year WMAP data together with other CMB results, and it is a prediction of the inflationary scenario. Nevertheless, we emphasize that it is an open experimental issue.

1.10.1 The geometry of the Universe.

The position of the first acoustic peak reveals that the Universe is flat or nearly so. As we describe above, the generation of acoustic peaks is governed by the (comoving) sound

horizon at decoupling, r_s (i.e., the greatest distance a density wave in the plasma could traverse, scaled to today's Universe). The sound horizon depends on ω_m, ω_b , and the radiation density, but not on $H_0, \Omega_k, \omega_\Lambda$, or the spectral tilt n_s . The peak positions versus angular multipole are then determined by $\Theta_A = r_s d_A^{-1}$, where the quantity d_A , the angular diameter distance, is the distance that properly takes into account the expansion history of the Universe between decoupling and today so that when d_A is multiplied by an observed angle, the result is the feature size at the time of decoupling. In a nonexpanding Universe, this would simply be the physical distance. The expression depends on the (evolution of the) content of the Universe. For a flat Universe, we have

$$d_A = \int_0^{z_{dec}} \frac{H_0^{-1} dz}{\sqrt{\Omega_r(1+z)^4 + \Omega_m(1+z)^3 + \Omega_\Lambda}}. \quad (5)$$

In this expression, Ω_r indicates the (well-known) radiation density, and the dilutions of the different components with redshift z , between decoupling and the present, enter explicitly.

1.10.2 Fitting for spectral tilt, matter, and baryon content.

It is easy to see how one in principle determines spectral tilt. If one knew all the other parameters, then the tilt would be found from the slope of the power spectrum after the removal of the other contributions. However, there is clearly a coupling to other parameters. Experiments with a very fine angular resolution will determine the power spectrum at very high l values, thereby improving the measurement of the tilt.

Here we discuss the primary dependences of the acoustic peak heights on ω_m and ω_b . Increasing ω_m decreases the peak heights. With greater matter density, the era of equality is pushed to earlier redshifts, allowing the dark matter more time to form deeper potential wells. When the baryons fall into these wells, their mass has less effect on the development of the potential so that the escaping photons are less redshifted than they would be, yielding a smaller temperature contrast. As to ω_b , increasing it decreases the second peak but enhances that of the third because the inertia in the photon-baryon fluid is increased, leading to hotter compressions and cooler rarefactions (16).

The peak-height ratios give the three parameters n_s, ω_m , and ω_b , with a precision just short of that from a full analysis of the power spectrum (discussed in Section 3.4.4). Following WMAP, we define the ratio of the second to the first peak by H_2^{TT} , the ratio of the third to the second peak by H_3^{TT} , and the ratio of the first to the second peak in the polarization-temperature cross-correlation power spectrum by H_2^{TE} . Table 1 shows how the errors in these ratios propagate into parameter errors. We see that all the ratios depend strongly on n_s , and that the ratio of the first two peaks depends strongly on ω_b but is also influenced by ω_m . For H_3^{TT} , the relative dependences on ω_b and ω_m are reversed. Finally, the baryon density has little influence on the ratio of the TE peaks. However, increasing ω_m deepens potential wells, increasing fluid velocities and the heights of all polarization peaks.

Table 1: Matrix of how errors in the peak ratios (defined in text) relate to the parameter errors.

	Δn_s	$\frac{\Delta \omega_b}{\omega_b}$	$\frac{\Delta \omega_m}{\omega_m}$
$\Delta H_2^{TT} / H_2^{TT}$	0.88	-0.67	0.039
$\Delta H_3^{TT} / H_3^{TT}$	1.28	-0.39	0.46
$\Delta H_2^{TE} / H_2^{TE}$	-0.66	0.095	0.45

Symbol	WMAP1	WMAP3	WMAP3 +other CMB	CMB + LSS	WMAP3 + SDSS
$\Omega_b h^2$	0.024 ± 0.001	0.02229 ± 0.00073	0.02232 ± 0.00074	$0.0226^{+0.0009}_{-0.0008}$	$0.02230^{+0.00071}_{-0.00070}$
$\Omega_m h^2$	0.14 ± 0.02	$0.1277^{+0.0080}_{-0.0079}$	0.1260 ± 0.0081	0.143 ± 0.005	$0.1327^{+0.0063}_{-0.0064}$
h	0.72 ± 0.05	$0.732^{+0.031}_{-0.032}$	$0.739^{+0.033}_{-0.032}$	$0.695^{+0.025}_{-0.023}$	0.710 ± 0.026
τ	$0.166^{+0.076}_{-0.071}$	0.089 ± 0.030	$0.088^{+0.031}_{-0.032}$	$0.101^{+0.051}_{-0.044}$	$0.080^{+0.029}_{-0.030}$
n_s	0.99 ± 0.04	0.958 ± 0.016	0.951 ± 0.016	0.95 ± 0.02	$0.948^{+0.016}_{-0.015}$

$\Omega_b h^2$: Baryon density, $\Omega_m h^2$: Matter density, h : Hubble parameter,
 τ : Optical Depth, n_s : Spectral index

Table 2: Results from six-parameter fits to CMB data, assuming a flat Universe and not showing the scalar amplitude A_s . Shown are results from first-year WMAP data, three-year WMAP data, and WMAP data combined with the bolometric experiments ACBAR and Boomerang. Fits using data from CBI and VSA (using coherent amplifiers) were also made, with consistent results. Also shown are results using LSS data with CMB data available in 2003, and from adding LSS data [from the Sloan Digital Sky Survey (SDSS)] to the WMAP3 data set (11). See Section 1.11 for appropriate references.

Table 2 lists the results from six-parameter fits to the power spectrum from several combinations of CMB data with and without complementary data from other sectors. The table includes results from Reference 14, which included most CMB data available at time of publication, and from even more recent analyses by WMAP (8).

1.11 Discussion of Cosmological Parameters

The overall conclusions from the analysis of the peak structure are not dramatically different from those drawn from a collection of earlier ground- and balloon-based experiments. Still, WMAP's first data release put the reigning cosmological model on much stronger footing. Few experiments claimed systematic errors on the overall amplitude of their TT measurements less than 10%; WMAP's errors are less than 0.5%. The overall amplitude is strongly affected by the reionization. With full-sky coverage, WMAP determined the power spectrum in individual l bins with negligible correlations. Now with the WMAP three-year data, results from higher-resolution experiments, and results on EE polarization, we are learning even more.

Remarkably, CMB data confirm the baryon density deduced from Big Bang nucleosynthesis, from processes occurring at approximately 1 s after the Big Bang: $\Omega_b h^2 = 0.0205 \pm 0.0035$. The determination of the nonzero density of dark matter at approximately 300,000 years reinforces the substantial evidence for dark matter in the nearby Universe. Finally, the flat geometry confirms the earlier (supernova) evidence of a dark energy component.

With temperature data alone, there is a significant degeneracy in parameter space, which becomes apparent when one realizes that there are just five key features in the power spectrum (at least with today's precision) to which one is fitting six parameters: the heights of three peaks, the location of the first peak, and the anisotropy on very large scales. The degeneracy can be understood as follows. The peak heights are normalized by the combination $A_s e^{-2\tau}$. Thus, both these parameters can increase in a way that leaves the peak heights unchanged, increasing the power on scales larger than the horizon at reionization. Increasing n_s can restore the balance but can also decrease the second peak. That peak can be brought back up by decreasing ω_b . WMAP broke this degeneracy in its

first-year release with a prior requiring $\tau < 0.3$. The new EE data from WMAP, in their sensitivity to reionization, break this degeneracy without the need for a prior.

Table 2 shows that the Hubble constant has been robust and in good agreement with determinations from Galaxy surveys. With better measurements of the peaks, the baryon and matter densities have moved systematically, but within error. The optical depth has decreased significantly and is now based upon the EE, rather than TE, power in the lowest l range. This change is coupled to a large change in the scalar amplitude. Finally, evidence for a spectral tilt ($n_s \neq 1$) is becoming more significant. As this is predicted by the simplest of inflationary scenarios, it is important and definitely worth watching.

The first-year WMAP data confirmed the COBE observation of unexpectedly low power in the lowest multipoles. The WMAP team reported this effect to be more significant than a statistical fluctuation, and lively literature on the subject followed. It is clear that the quadrupole has little power and appears to be aligned with the octopole. However, the situation is unclear in that the quadrupole lines up reasonably well with the Galaxy itself, and there is concern that the cut on the WMAP data to remove the Galaxy then reduced the inherent quadrupole power. The anomaly has been reduced with the three-year data release, with improvements to the analysis, particularly in the lowest multipoles.

Table 2 also gives results from fitting CMB data with data from other cosmological probes, in particular large-scale structure (LSS) data in the form of three-dimensional Galaxy power spectra (the third dimension is redshift). Such spectra extend the lever arm in k space, allowing a more incisive determination of any possible spectral tilt, n_s . However, there are potential biases with the Galaxy data. In particular, the galaxies may not be faithful tracers of the dark matter density. Already before the three-year WMAP data release, including LSS data with CMB data favored an optical depth closer to its current value and provided evidence of spectral tilt. With three-year WMAP data and the Sloan Digital Sky Survey Galaxy survey data, the significance of a nonzero tilt is near the 3σ level. This is a vigorously debated topic. There are other LSS surveys that give similar and nearly consistent results, yet the systematic understanding is not at the level where combining all such surveys makes sense.

1.11.1 Beyond the six basic parameters.

With the LSS data, one can obtain information on other parameters that were held fixed. In particular, relaxing the constraint on Ω_k , one finds consistency with a flat Universe to the level of approximately 0.04 (with CMB data alone) and 0.02 (using LSS data) (see Reference 14). Using WMAP and other surveys, constraints as low as 0.015 are obtained with some sets, giving slight indications for a closed Universe ($\Omega_k < 0$).

There is sensitivity to the fraction of the dark matter that resides in neutrinos: f_ν . The neutrino number density (in the standard cosmological model) is well known; a mean neutrino mass of 0.05 eV corresponds to Ω_ν of approximately 0.001. The current limits are $\bar{M}_\nu < 1$ eV from the CMB alone and $\bar{M}_\nu < 0.4$ eV when including Galaxy power spectra (14).

One can also extract information about the dark energy equation-of-state parameter w . If dark energy is Einstein's cosmological constant, then $w \equiv -1$. Because w affects the expansion history of the Universe at late times, the associated effects on power spectra then give a measure of w . Using all available CMB data, Reference 14 finds $w = -0.86_{-0.36}^{+0.35}$. However, by including both the Galaxy power spectra and SN1A data, the stronger constraint $w = -0.94_{-0.097}^{+0.093}$ is derived. WMAP, using its own data and another collection of LSS data together with supernova data, finds $w = -1.08 \pm 0.12$, where in this fit they also let Ω_k float.

Finally, we want to mention a new effect, even if outside the domain of the CMB baryon

oscillations. In principle, one should be able to see the same kind of acoustic oscillations in baryons (galaxies) seen so prominently in the radiation field. If so, this will provide another powerful measure of the effects of dark energy at late times, specifically the time when its fraction is growing and its effects in curtailing structure formation are the largest. This effect has recently been seen (17) at the level of 3.4σ , and new experiments to study this far more precisely are being proposed. This is an excellent example of how rapidly the field of observational cosmology is developing. In the wonderful textbook *Modern Cosmology* by Scott Dodelson (2, p. 209), Dodelson states that this phenomenon would only be barely (if at all) detectable.

Before turning to a discussion of the problem of astrophysical foregrounds, we mention that currently the utility of ever more precise cosmological-parameter determination is, like in particle physics, not that we can compare such values with theory but rather that we can either uncover inconsistencies in our modeling of the physics of the Universe or gain ever more confidence in such modeling.

2 FOREGROUNDS

Until now, we have introduced the features of the CMB, enticing the reader with its promises of fascinating insights to the very early Universe. Now we turn our attention toward the challenge of actually studying the CMB, as its retrieval is not at all an easy endeavor. Instrumental noise and imperfections could compromise measurements of the tiny signals (see Section 3). Even with an ideal receiver, various astrophysical or atmospheric foregrounds could contaminate or even suppress the CMB signal. In this section we first give an overview of the relevant foregrounds, then describe the options for foreground removal and estimate their impact.

2.1 Overview

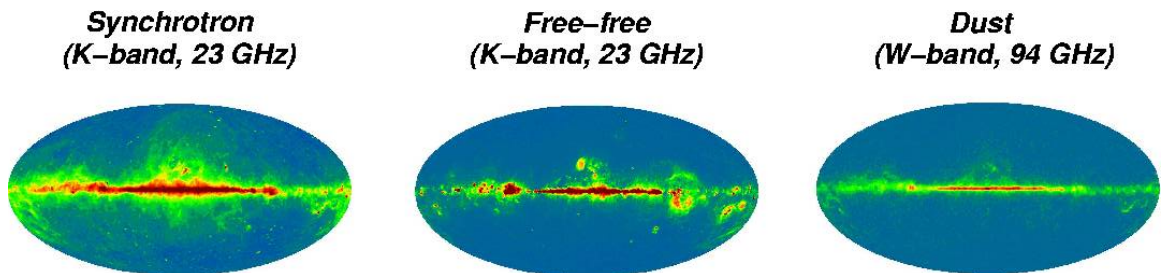


Figure 7: Unpolarized foreground maps in Galactic coordinates, derived from WMAP. Each map is shown at the WMAP frequency band in which that foreground is dominant. The color scale for the temperature is linear, with maxima set at approximately 5 mK for K-band and 2.5 mK for W-band. Images courtesy of the WMAP science team.

One may be tempted to observe the CMB at its maximum, approximately 150-200 GHz. However, atmospheric, galactic, or extragalactic foregrounds, which have their own dependences on frequency and angular scale, may dominate the total signal, so the maximum may not be the best choice.

The main astrophysical foregrounds come from our own Galaxy, from three distinct mechanisms: synchrotron radiation; radiation from electron-ion scattering, usually referred to as free-free emission; and dust emission. Figure 7 displays full-sky intensity maps for the main foreground components as derived from WMAP data at microwave

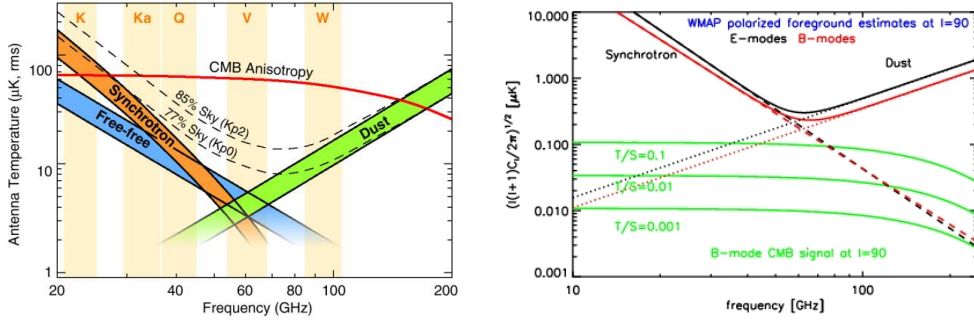


Figure 8: Frequency dependence of foregrounds recorded in antenna temperature. (a) The rms on angular scales of 1 for the unpolarized CMB compared with that from foregrounds extracted from the WMAP data (18). The WMAP frequency bands (K, Ka, Q, V, W) are overlaid as light bands. These plots are for nearly full sky; the total foregrounds are shown as dashed lines for two different sky cuts. Figure courtesy of the WMAP science team. (b) A similar plot of the expected polarization level of foregrounds at $l = 90$ in comparison with that from primordial B modes (which peak around $l = 90$) for different values of r following formula 25 in Reference 19. Again, these estimates are for observations covering most of the sky.

frequencies where the bright Galaxy is clearly dominating the pictures. Each component is shown for the WMAP frequency channel where it is dominant.

Figure 8 compares the expected CMB signal as a function of frequency to the rms of WMAP foreground maps on an angular scale of 1° . The ordinate axis records antenna temperature (see Section 3.2.1). An optimal observing frequency range with the highest ratio of CMB to foreground signal is in the region around 70 GHz (often termed the cosmological window).

Much less is known about the polarization of foregrounds. Information is extrapolated mostly from very low or very high frequencies or from surveys of small patches. Figure 8b shows an analog figure for the polarization fluctuations as estimated from WMAP three-year data on an angular scale of approximately 2° ($l = 90$), where the signal from gravitational waves is maximal. The dust estimate has some limitations because the WMAP frequency channels do not extend to the high frequencies where the dust is expected to dominate the foregrounds.

The expected B-mode signal is smaller than the estimated foreground signal even for $r = 0.1$. However, almost the full sky was used for the estimate, whereas recent studies (20, 21) using lower-frequency data and WMAP data indicate that the polarization of synchrotron radiation on selected clean patches can be significantly smaller. Thus, the optimal frequency window will shift depending on which region is observed. After discussing possible foreground effects from Earth’s atmosphere, we briefly review what is known about the dominant sources of galactic and extragalactic foregrounds.

2.1.1 Atmospheric effects.

The atmosphere absorbs short-wavelength radiation, but fortunately has transmission windows in the range of visible light and microwave radiation. Absorption lines from oxygen (around 60 and 120 GHz) and water vapor (20 and 180 GHz) limit the access to the microwave sky, and, in particular, clouds and high water vapor can compromise ground-based observations. Thermal emission from the atmosphere can add significantly to the

observed signal for ground-based experiments (depending on the observing site and the frequency, from 1-40 K) and, together with the instrumental noise and/or thermal emission from warm optical components, can make for the major part of the detected power (see also Section 3.2.1). The observing strategy needs to be designed in a way that allows a proper removal of the varying atmospheric contribution without a big impact on the signal extraction (see also Sections 3.3 and 3.4.1).

Although thermal emission from the atmosphere is unpolarized, the Zeeman splitting of oxygen lines in Earth's magnetic field leads to polarized emission, which is dominantly circularly polarized. Although the CMB is not expected to be circularly polarized, Hanany & Rosenkranz (22) showed that for large angular scales, $l \approx 1$, a 0.01% circular-to-linear polarization conversion in the instrument could produce a signal more than a factor of two higher than the expected gravitational wave B-mode signal if r were small, that is, if $r = 0.01$.

In addition, backscattering of thermal radiation from Earth's surface from ice crystal clouds in the upper troposphere may give signals on the order of micro-Kelvin size (23), again larger than the expected B-mode signal. Although the polarized signal from oxygen splitting would be fixed in Earth's reference frame, and thus could be separated from the CMB, the signal from such ice clouds would reflect the varying inhomogeneous cloud distribution and thus be hard to remove.

2.1.2 Galactic synchrotron radiation.

Synchrotron radiation is something familiar to particle physicists, mostly from storage rings where some of the energy meant to boost the particle's energy will be radiated away. The same effect takes place in galactic accelerators, with cosmic-ray electrons passing through the galactic magnetic field. In contrast to the particle physics case, where electrons of energies of a few GeV pass magnetic elds of up to a few 1000 G, we are dealing here with electrons in a galactic field of only a few micro-Gauss.

This component of the foreground radiation is dominant at frequencies below 70 GHz, and its intensity characteristics have been studied at frequencies up to 20 GHz. The frequency and angular dependence both follow power laws $T \propto \nu^{-\beta}$, with a position- and frequency-dependent exponent that varies between 2 and 3.

Theoretically, a high degree of sychrotron polarization ($> 75\%$) is expected, but low-frequency data imply much lower values. However, at low frequencies, Faraday rotation where light traversing a magnetized medium has its left and right circular polarized components travel at different speeds reduces the polarization.

2.1.3 Galactic dust.

Interstellar dust emits mainly in the far infrared and thus becomes relevant for high frequencies ($\nu > 100$ GHz). The grain size and dust temperature determine the properties of the radiation, where the intensity follows a power law $T \propto T_0 \nu^\beta$, with the spectral index $\beta \approx 2$ and with both T_0 and β varying over the sky. Using far-infrared data from COBE, Finkbeiner et al. (24) (FDS) provided a model for the dust emission consisting of two components of different temperature and emissivity ($T = 9.4/16$ K, $\beta = 1.67/2.7$).

There are also indications for another component in the dust emission, as seen through cross correlation of the CMB and far-infrared data. Its spectral index is consistent with free-free emission, but it is spatially correlated with dust. This anomalous dust contribution could derive from spinning dust grains. However, current data do not provide a conclusive picture, and additional data in the 5-15-GHz range are needed to better understand this component (25). In 2003, the balloon-borne experiment ARCHEOPS reported 5% to 20% polarization of the submillimeter diffuse galactic dust emission, providing the

first large coverage maps of polarized galactic submillimeter emission at 13' resolution (26). More recently, they also published submillimeter polarization limits at large angular scales, which when extrapolated to 100 GHz are still much larger than the expected gravitational wave signal for $r = 0.3$ (27).

2.1.4 Free-free emission.

Electron-ion scattering leads to radiation that is, in this context, termed free-free emission, whereas in the high-energy lab, it is better known as bremsstrahlung. This component does not dominate the foregrounds at any radio frequency. Sky maps of free-free emission can be approximated using measurements of the H α emission (from the hydrogen transition from $n = 3$ to $n = 2$), which traces the ionized medium. The thermal free-free emission follows a power law $T \propto \nu^{-\beta}$, where $\beta \approx 2$. This foreground is not polarized.

2.1.5 Point sources.

Known extragalactic point sources are a well-localized contaminant and easily removable. However, the contribution from unresolved point sources can severely affect measurements: for example, the recent discussion of their impact on the determination of n_s from WMAP-data (28). Point sources impact CMB measurements mostly at high angular scales and low frequencies. For low frequencies, their contribution may still be larger than the signal expected from gravitational waves.

2.2 Foreground Removal

Understanding and removing foregrounds are most critical for the tiny polarization signals. The different frequency dependences of the CMB and galactic foregrounds provide a good handle for foreground removal using multifrequency measurements.

For the polarization analysis, methods where little or no prior information is required are the most useful for now. A promising strategy is the Independent Component Analysis, which has already been applied to several CMB temperature data sets (including COBE, BEAST, and WMAP) and for which formalism has also been developed to cope with polarization data. The foreground and CMB signals are assumed to be statistically independent, with at least one foreground component being non-Gaussian. Then the maximization of a specific measure of entropy is used to disentangle the independent components. Stivoli et al. (29) demonstrated a successful cleaning of foregrounds using simulated data. Verde et al. (30) estimated the impact of foregrounds independent of removal strategy, considering different degrees of effectiveness in cleaning. A 1% level of residual foregrounds, in their power spectrum, was found to be necessary to obtain a 3σ detection of $r = 0.01$ from the ground.

Because all current studies rely on untested assumptions about foregrounds, they need to be justified with more data. Moreover, none of the studies to date takes into account the impact of foregrounds in the presence of lensing and instrumental systematics. Work is needed on both the experimental and theoretical side to obtain a more realistic picture of the foregrounds and their impact.

3 METHODS OF DETECTION

We have argued that in the patterns of the CMB lies greatness; here we outline the essential ingredients for measuring CMB anisotropies. The fundamental elements for detecting microwave emission from the celestial sphere are optics and receivers. The optics comprises telescopes and additional optical elements that couple light into the receivers. The

receivers transduce the intensity of the incoming microwave radiation into voltages that can be digitized and stored. Two other CMB experiment requirements are fidelity control (calibration and rejection of spurious signals) and optimized strategies for scanning the telescope beams across the rotating sky. Below, after a general introduction to the problem, we elaborate on these topics and culminate with an overview of data analysis techniques.

3.1 The CMB Experiment Basics

All CMB experiments share certain characteristics. Some main optical element determines the resolution of the experiment. This main optical element may be a reflecting telescope with a single parabolic mirror, or one with two or more mirrors; it may be a refracting telescope using dielectric lenses; it may be an array of mirrors configured as an interferometer; it may be just a horn antenna². In most cases, additional optical elements are required to bring the light to the receiver. Examples include Dewar windows, lenses, filters, polarization modulators, and feedhorns (which are horn antennas used to collect light from telescopes). Typically these coupling optics are small enough that they can be maintained at cryogenic temperatures to reduce their thermal emission and lossiness.

The low-noise receivers are nearly always cryogenic and divide into two types, described below. Spatial modulation of the CMB signal on timescales of less than one minute is critical to avoid slow drifts in the responsivity of the receivers, and may proceed by movement of the entire optical system, or by moving some of its components while others remain fixed. Large ground screens surround most experiments to shield the receivers from the 300-K radiation from Earth. Typically, the thermal environment of the experiment must be well regulated for stability of the receiver responsivity and to avoid confusion of diurnal effects from the environment with the daily rotation of the celestial signal. Earth-bound experiments suffer the excess noise from the atmosphere, as well as its attenuation of the signal, and must contend with 2π of the 300-K radiation. Balloon-borne experiments suffer less atmosphere, but must be shielded from the balloon's thermal radiation and typically have limited lifetimes (1-20 days). Long flights usually require constant shielding from the Sun during the long austral summer day. Space missions have multiple advantages: no atmosphere, Earth filling a much less solid angle, a very stable thermal environment, and a longer lifetime than current balloon missions.

3.2 The Detection Techniques

Although to fully describe the CMB anisotropies requires their spatial power spectra (which happily are not white), a useful order-of-magnitude number is that the rms of the CMB sky when convolved to 10° scales is approximately $30 \mu\text{K}$, and approximately $70 \mu\text{K}$ for 0.7° scales (the first acoustic peak). This rms of the CMB temperature is some 20 ppm of the 2.7-K background, the polarization E modes are 20 times lower, and the primordial B-mode rms is predicted to be 50 ppb or less.

A microwave receiver measures one or more of the Stokes parameters of the radiation incident on it. Two classes of low-noise receivers may be identified: coherent receivers, in which phase-preserving amplification of the incident field precedes detection of its intensity, and incoherent receivers, in which direct measurement of the intensity of the incident field is performed.

In coherent receivers, the incident field is piped around transmission lines as a time-varying voltage. That voltage is amplified in transistor amplifiers, and then the signal is

²A horn antenna is waveguide flared to the appropriate aperture for the desired resolution; these were used in the COBE satellite instrument that made the first detection of CMB anisotropy.

eventually detected when it passes through a nonlinear element (such as a diode) with an output proportional to the square of the incident field strength. The critical element in the coherent receiver is not the detector but typically the transistor amplifier, which must be a low-noise amplifier. In cases where transistor amplifiers are not available at high enough frequencies, the first and most critical element in the receiver is a low-noise mixer, which converts the frequency of the radiation to lower frequencies, where low-noise amplifiers are available.

For the CMB, the most widely used incoherent detector to date is the bolometer. A bolometer records the intensity of incident radiation by measuring the temperature rise of an isolated absorber of the radiation. A promising effort is underway to develop receivers in which the bolometers are coupled to transmission lines, where they can serve as the very low-noise detectors in what otherwise looks like a coherent receiver.

3.2.1 Calibration, Kelvins, and system temperature.

A microwave receiver outputs a voltage proportional to the intensity I of the incident radiation over some effective bandwidth $\Delta\nu$ centered on frequency ν_0 . The output is calibrated in temperature units through observation of blackbody sources. The polarization anisotropies of the CMB are also described in temperature units. This follows because the Stokes parameters Q and U have the same units as the intensity I . There is a factor of two to keep track of: The usual definition of I sums the intensities from two orthogonal polarization modes. Note that the antenna temperature T_A is defined by the approximation $I \propto T_A$. Only in the Rayleigh-Jeans regime of a blackbody does $T_A \approx T$, but it is a convenient measure for comparing the effects of various foregrounds and other contaminants.

Microwave receivers are sensitive to the total intensity of the incident radiation over the bandpass. The incident electric field can be considered as a sum of incoherent (i.e., uncorrelated) sources, each with intensity that can be associated to a temperature in the Rayleigh-Jeans limit. Thus, we can define the system temperature to describe the input power to the receiver:

$$T_{sys} = T_{CMB} + T_{fg} + T_{atm} + T_{gnd} + T_{opt} + T_n, \quad (6)$$

where we have included terms for the CMB, foregrounds, atmosphere, 300-K emission from the ground, emission from the warm optics, and receiver, respectively. We do not note explicitly that the extra-atmospheric signals are attenuated slightly as they pass through the atmosphere. At good sites such as the Atacama Desert in Chile or the South Pole, this effect is small for $\nu = 110$ GHz. We also neglect absorption in the optics, although in bolometer systems, this effect can be large. Note that when describing bolometer receivers, it is more common to leave the sum in units of power, as we see below.

3.2.2 Sensitivity and noise.

Imagine a CMB experiment that scans across a small enough region of sky that the sky curvature may be neglected, recording the temperature of each of N beam-sized patches of sky a single time into a vector d . The error on each measurement is σ_e . Let us first take the (unattainable) case where $\sigma_e \ll 1$ nK. In that case, σ_d measures the variance of the CMB itself. If the CMB power spectrum were white with average level ΔT^2 , for example, the variance could be crudely estimated as

$$\sigma_d^2 \approx \Delta T^2 \frac{\delta l}{l_c}, \quad (7)$$

where l_c is some average in the region δl between $(x_b)^{-1}$ and $(Nx_b)^{-1}$, with x_b the diameter of the beam-sized patch in radians. Typical numbers might give $\delta l/l_c \approx 1$, and $\Delta T = 60\mu\text{ K} \approx \sigma_d$. Thus, for σ_e so small, one could estimate the Fourier modes (or the C_l themselves) directly and trace out details of the spectrum over the range δl .

To consider a more realistic case, we note that CMB receivers are characterized according to their sensitivity S in units of $\text{K}\sqrt{\text{s}}$. The variance σ_T^2 of a series of measurements, each resulting from an integration time τ , is then found by $\sigma_T^2 = S/\tau$. A typical value for the sensitivity of a single receiver is $500\ \mu\text{K}\sqrt{\text{s}}$, so that after 10 min on each patch, one might attain $\sigma_e \approx 20\mu\text{K}$ and then detect the CMB signal excess variance in the data. Typical variances in the CMB E polarization are $(4\ \mu\text{K})^2$, so these experiments must integrate for hundreds of hours and/or use hundreds of receivers. The tougher sensitivity requirements for B modes are described in Section 4.

In cases where the mean photon mode occupancy n_0 for the input radiation is large, $n_0 = (e^x - 1)^{-1} \gg 1$ with $x = h\nu/(kT_{sys})$, we can describe classically the sensitivity of an ideal direct receiver of bandwidth $\Delta\nu$ with the Dicke equation: $S = T_{sys}/\sqrt{\Delta\nu}$. We account for more complex receivers below. Most coherent receivers operate in the limit $n_0 \gg 1$. In cases where $n_0 \ll 1$ (low T_{sys} and high frequency ν), the limitation to sensitivity in ideal bolometric receivers comes from photon shot noise (counting statistics), and the sensitivity depends on T_{sys} in cases where the bolometer thermal noise is negligible. We return to the noise in bolometers below.

The sensitivity of the receiver captures its best features succinctly. It is also instructive to look at the spectra of postdetection signal noise from the receivers. The scanning of the telescope translates the CMB anisotropy signal to variations in time that lie atop the intrinsic postdetection noise. A typical noise power spectrum is shown in Figure 9. This spectrum shows a white-noise level at frequencies $f > 0.01$ Hz; the sensitivity is measured from the white noise. The spectrum also shows characteristic low-frequency noise approximately proportional to $1/f$, which can be parametrized by the frequency f_c where the $1/f$ and white-noise powers are equal. Such $1/f$ noise is ubiquitous; the atmosphere itself has a $1/f$ spectrum. In principal, this noise is quite serious, as it contributes more and more to the variance with longer integration times. In practice, experiments are designed to modulate the signal at frequencies $f > f_c$. Usually the receiver includes a low-pass filter that limits the bandwidth of the postdetection data stream to f_{Ny} . Then these data are Nyquist sampled and digitized at a rate of $2f_{Ny}$ to avoid aliasing high-frequency noise. Roughly speaking, the postdetection bandwidth of interest is usually between 0.01-0.1 Hz and 50-200 Hz.

3.2.3 Coherent receivers.

A key advantage of coherent receivers is that they can be configured so that their output is the correlation of two input signals. We devote the bulk of our discussion here to this topic.

Coherent-receiver noise spectra. The noise properties of amplifiers include both intrinsic output voltage fluctuations, present in principle even in the absence of input signal³ and characterized by T_n , and fluctuations in the gain coefficient (the factor by which the input voltage is amplified). An extension of the Dicke equation reads

$$\delta T = aT_{sys} \sqrt{\frac{1}{\Delta\nu\tau} + \left(\frac{\delta g}{g}\right)^2}, \quad (8)$$

³We remind the reader that for the frequencies of interest, absence of input signal is a difficult requirement because a resistive termination emits thermal radiation, whereas a shorted input reflects back any thermal radiation emitted from the amplifier input.

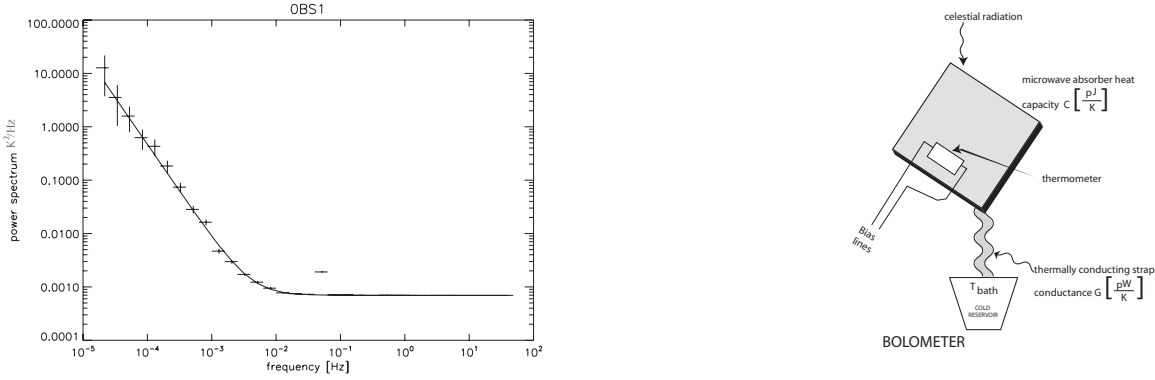


Figure 9: (Left) Raw postdetection noise power spectrum from a correlation polarimeter during scans of the sky, illustrating three interesting features: its white-noise level at frequency $f > 0.01$ Hz, a peak corresponding to the scan period of 21 s, and the characteristic low-frequency noise with slope $1/f$. Figure courtesy of C. Bischoff and the CAPMAP team (31). (Right) Sketch of a bolometer, indicating that celestial radiation is absorbed in a material with heat capacity C coupled to a cold reservoir at temperature T_{bath} by a strap with low thermal conductance G . A thermometer measures the power delivered to the absorber by recording its temperature increase.

where the coefficient a depends on the exact configuration of the receiver; $a = 1$ for a direct receiver in which the input is amplified and then detected. For the correlation polarimeters described below, $a = \sqrt{2}$.

Signal correlation. Two signals are correlated if the time average of their product is nonzero. In 1952, Ryle (32) introduced the concept of phase switching: periodically introducing a half-wavelength phase lag into one of the two signal lines, which changes the sign of the correlation product. Then, one can sum the two inputs and square them in a detector diode. The correlation product is now modulated at the phase-switching rate and may be recovered. The correlation can also be measured in analog correlators (multipliers) or by digitization of the inputs, followed by multiplication.

Correlation receivers. Correlation receivers have been used in several ways to measure CMB signals. We describe two methods below. The advantages of correlation include reduced sensitivity to $1/f$ variations in amplifiers (because phase switching with diode switches can be effected at kilo-Hertz rates), reduced sensitivity to gain fluctuations (because those fluctuations multiply only the small correlated signal rather than the large, common-mode intensity signal), and the ability to access all four of the Stokes parameters that describe the full polarization state of the radiation using only two inputs.

Interferometers. Perhaps the best-known example of signal correlation in astronomy lies in the interferometer, which uses the correlation of signals from two spatially separated telescopes to measure Fourier modes of the celestial radiation in a limited field of view. The interferometer's receiver detects a slice of the interference pattern that arises when the two input signals originate with phase coherence, much as the screen in a Young's diffraction experiment does. The angular resolution is determined by the spacing between the telescopes, whereas the size of the individual telescopes limits the field of view. The resolution of an interferometer may be described in terms of its synthesized beamwidth,

σ_b . Because the CMB is an extended source, nearly all the Fourier modes in the field of view are needed to fully characterize it. All the Fourier modes can be measured only if the individual telescopes are close packed so that they fill all the space required for an equivalent single dish of resolution σ_b .

To recover all four Stokes parameters, the telescope optics usually includes circular polarizers so that a given receiver amplifies either the left (L) or right (R) circular polarization state. Both DASI and CBI used quarter-wave plates in the optics to periodically reverse the polarization state, $L \leftrightarrow R$, so that all possible combinations of correlations (LR , LL , RR , and RL) could be measured from each pair of telescopes.

Correlation polarimeters. In a correlation polarimeter, the incident signal enters through an azimuthally symmetric feedhorn and is separated into two polarization states (either two orthogonal linear polarization states or the L and R circular polarization states) before amplification in high-electron-mobility-transistor amplifiers. After amplification, the two polarization states are correlated so that the output is proportional to a linear Stokes parameter: $V_{out} \propto \pm E_x E_y \propto \pm U$, with the modulation provided by the phase switch. Figure 9 shows the stability of a phase-switched correlation polarimeter, switched at 4 kHz. The high-electron-mobility-transistor amplifiers in this polarimeter have $1/f$ knees at 1 kHz and cannot be used without this rapid modulation. The sensitivity of this polarimeter is found from the Dicke equation with $a = \sqrt{2}$. If L and R states are used, then the second linear Stokes parameter can also be obtained by phase shifting R by an extra $\pi/2$ and then correlating it with L . The correlation can come about either through direct multiplication of the two polarization states or through the Ryle technique. The QUIET project uses the latter method, in which L and R are sent into a compact module that mounts onto a circuit board. The correlation LR is constructed by differencing the squares of the sum and difference terms $L + R$ and $L - R$; U is found by similar means. Phase switches at 4 kHz modulate the outputs, which are read out on module pins; other module pins are used to bias the amplifiers.

3.2.4 Incoherent detectors.

A number of clever ideas beyond the scope of this review are being pursued for tailoring bolometers to search for CMB polarization. One recent great success was the advent of the polarization-sensitive bolometer. Another avenue is using wafer-level silicon fabrication techniques to produce arrays of hundreds of detectors at once, sometimes coupling the detectors directly to planar antennas or antenna arrays (antenna-coupled bolometers). Below we focus on the rudiments of the transition edge sensor (TES) bolometer. Figure 9 depicts the critical elements of a bolometer. Celestial radiation impinges on a microwave absorber with heat capacity C . The absorber is connected to a cold reservoir at temperature T_{bath} by a thermal strap of heat conductance G . A fluctuation in the intensity of the celestial radiation warms the absorber slightly. This temperature change is recorded by a thermometer, typically a material with a large-magnitude logarithmic derivative $d \log R / d \log T \equiv \alpha$ of resistance with respect to temperature.

Transition edge sensor bolometers. The TES is a superconductor maintained at its critical temperature T_c . We describe the TES as being on (or in) the transition when its resistance is between zero and the normal resistance R_n . For CMB devices optimized to work with $T_{bath} \approx 300$ mK, a typical critical temperature is $T_c \approx 400 - 500$ mK. The width of the transition is typically a percent of T_c . Many TESs comprise a bilayer: a thin layer of natural superconductor topped with normal metal. The T_c and R_n of bilayers can be controlled by varying the two thicknesses.

The TES is operated in series with an ideal inductor L . To voltage bias the TES at operating resistance R_0 , a small shunt resistance $R_{sh} \ll R_0$ is placed in parallel with the TES/inductor combination and fed with a bias current. Fluctuations in R_0 cause current fluctuations through the inductor. Flux through the inductor is linked to a superconducting quantum interference device (SQUID), which serves as a current amplifier. To prevent the SQUID current noise from contributing significantly, the operating resistance R_0 is kept low: $R_0 < 1\Omega$.

The voltage bias causes the TES resistor to dissipate heat. Rough order-of-magnitude values for TES bolometers used for the CMB may be $G \approx 30 \text{ pWK}^{-1}$ and $C \approx 0.3 \text{ pJ K}^{-1}$. The thermal timescale for the bolometer to change temperature in response to a fluctuation in the photon power is $\tau_{th} = C/G \approx 10 \text{ ms}$, corresponding to a one-pole low-pass filter at $f = (2\pi\tau)^{-1} \approx 15 \text{ Hz}$. Conceptually, we note that when a fluctuation in the photon noise warms the bolometer, the TES resistance increases, as $\alpha > 0$. Because the TES is voltage biased, the increase in resistance lowers the Joule heating power V^2/R flowing into the bolometer. These electrical changes can occur more quickly than the thermal timescale τ_{th} . This is the phenomenon of electrothermal feedback, which speeds up the TES bolometer and also stabilizes it so that it stays in its transition.

TES bolometer noise spectra. In Section 3.2.2 we considered the sensitivity of an instrument in the case of photon occupancy number $n \ll 1$ and mentioned that the sensitivity is then proportional to $\sqrt{T_{sys}}$, or, more appropriately because $n \ll 1$ contraindicates the Rayleigh-Jeans approximation, to \sqrt{P} , where P is the power in the incident radiation field, also known as the photon power. In the general case for CMB experiments, $n \approx 1$, and so a more general formula is required (see Reference 33 for a discussion).

For bolometers, the receiver sensitivity is usually described in terms of the noise-equivalent power (NEP) that can be measured in a postdetection bandwidth of 1 Hz. NEP properly has units not of power, but of W/\sqrt{Hz} . A bandwidth of 1 Hz is equivalent to a half-second of integration time. Besides this factor, converting to units of $\mu\text{K}\sqrt{s}$ appropriate for detecting CMB fluctuations requires the appropriate derivative to convert power to thermodynamic temperature and requires referencing the NEP to the entrance of the optics. (In practice, the second point means correcting for the efficiency $\eta < 1$ in a high-frequency system).

The total NEP^2 for a receiver can be found by summing up the squares of NEPs from different terms, of which the contribution from photons, NEP_γ , is only one. When NEP_γ dominates the sum, the detector is said to be background limited. Intrinsic sources of noise in bolometer systems include thermal noise from the photons transporting heat to the cold bath ($\text{NEP}_{th} \approx \sqrt{2kT_0^2G}$), Johnson noise power in the bolometer resistance (which is reduced significantly by the electrothermal feedback, as described in Reference 34), back-end noise (from the SQUIDs), and occasional other unexplained sources of noise, including $1/f$ noise.

The inductor in series with the TES resistor serves not only to couple the TES current to the SQUID output, but also to provide a Nyquist filter with time constant L/R_0 . The L/R_0 time constant low pass filters the signals, and the noise power, before they emerge from the cryostat. Now that we have reviewed the experimental basics and detectors used for CMB measurements, we turn to the discussion of how to choose an observing strategy for an experiment.

3.3 Observing Strategies

We are surrounded by a bath of CMB photons, and with all directions being equal it seems that only astrophysical foregrounds determine the choice for which parts of the sky

should be observed. The size of the observed patch, together with the angular resolution, determines the accessible angular scales. However, the size, shape, and uneven coverage of the observed region, and even the way in which it is scanned, all impact the determination of the CMB power spectrum so that an optimization of the observing strategy requires more sophisticated considerations. A pedagogical illustration of the choices and their impacts is given in Reference 35. We mention here the most important issues that must be taken into account in developing an observing strategy.

Including the cosmic variance (see Equation 2), the achievable precision in the power spectrum (C_l) can be expressed in the following form:

$$\frac{\Delta C_l}{C_l} = \sqrt{\frac{2}{2l+1}} \left(\frac{1}{\sqrt{f_{sky}}} + \frac{4\pi(T_{exp})^2}{C_l} \sqrt{f_{sky}} e^{l^2 \sigma_b^2} \right). \quad (9)$$

Here, f_{sky} represents the observed fraction of the sky, T_{exp} the total experimental sensitivity (ΔT combining all detectors for the duration of the run), and σ_b the width of the beam. Finite beam resolution degrades the sensitivity progressively more at higher l values. For example, the WMAP beam of approximately 0.2° limits sensitivity to below $l \approx 600$; smaller beams are needed to study much finer scales. In general, the impact of the scanning strategy on the measurement of the different C_l is summarized in a window function that describes the weight with which each C_l contributes to the measured temperatures. A crude estimate of the lowest accessible l is $l_{min} \approx 1/\Delta\Theta$, with Θ being the angular extent of the survey. Limited sky coverage leads to correlations in the power at different multipoles l . Therefore, the power spectrum is usually reported in largely uncorrelated l bands of width Δl , which should be larger than l_{min} . The error on the average C_l in an l band then follows from Equation 9, with a prefactor of $1/\sqrt{\Delta l}$.

For an experiment to optimally take advantage of its sensitivity ΔT , the size of the observed sky patch should be chosen such that the contributions to the uncertainty in C_l from sample variance (first summand) and from noise (second summand) are roughly equal. This leads to $4\pi f_{sky} = C_l e^{-l^2 \sigma_b^2} (\Delta T)^{-2}$. Another way to express this is that the ideal patch size is such that the signal-to-noise ratio per pixel $\sigma_{CMB}/(\Delta T_{pix})$ is unity, where σ_{CMB} is the expected CMB fluctuation in a beam-sized pixel and T_{pix} the experimental error on the temperature in that pixel.

A polarization analysis always suffers from small survey sizes because E and B modes are not local fields, and thus a small patch contains ambiguous modes. The power spectrum estimation can then lead to E-to-B leakage and distort the B-mode measurements. Because the CMB B modes are an order of magnitude smaller than the E modes, even a small leakage can significantly affect the measurements. However, Smith (36) has already demonstrated a method for avoiding significant leakage.

In an optimal experiment, the observed patch is covered homogeneously, which maximizes the sensitivity to the power spectrum for a given integration time. It is beneficial to cover any pixel in the observed patch with different receivers, and also with different receiver orientations, especially but not only for the polarization analysis. This cross linking provides robustness against effects from time-stream filters in the data processing (see Section 3.4.1) and enables various systematic studies where instrumental effects or pickup of signals from the ground can be distinguished from real signals on the sky (see Reference 37 for another view on this).

Using a purely azimuthal scan on a patch, the atmospheric contribution is constant, but polarization-sensitive receivers detect different combinations of Q and U at different times, leading to pixels having nonuniform weights for Q and U . This also compromises the disentanglement of E and B modes, reducing sensitivity. A more symmetric distribution is achieved by scanning, for example, in a ring pattern, resulting in much more uniform Q/U sensitivity and enabling many systematic cross checks with a high degree of symmetry.

However, a changing atmospheric contribution along the ring must then be taken into account.

For any experiment, the scan speed should be as fast as possible to decrease the effects of $1/f$ drifts (see Section 3.2.2), but upper limits are posed by the beam resolution, maximum sampling speed, mechanical constraints of the telescope, and detector time constants. Typical scanning speeds are tens of arcminutes per second. Typical sampling at 10-100 Hz then provides several samples per beam. Given all the above considerations, it is clear that an optimization of the observing strategy is not trivial and any scan strategy will include some compromises. So far we have discussed the challenges in acquiring useful CMB data. In the next section we introduce the obstacles still lying ahead in the processing of data to enable access to its cosmological treasures.

3.4 Techniques of Data Analysis

In CMB experiments, data are accumulated continuously over a duration ranging from a few hours (balloon experiments) up to a few years (space missions). The data volume for past and current experiments was at most a few hundred gigabytes. Even with planned expansions to arrays of ~ 1000 receivers, the data streams will amount to a fraction of typical current high-energy physics experiments: 10-50 Tbytes per year. Although for high-energy physics experiments the data records can be split into different categories of interest and the analyses are usually performed on specific selections of the data with an event-wise treatment, here all of the acquired data contain the same signal and the signal's extraction becomes possible only with long integration times, requiring the processing of all data in the same analysis. Typically the CMB analysis can be divided into four main steps, which are described in the following sections.

3.4.1 Filtering and cutting.

Imaging the CMB requires careful cleaning of the data. Selection of data without instrumental failures or bad weather (for groundbased experiments) comprises the first filter on the data. The detector time streams contain long-term drifts of the detector responsivities and often of the atmosphere, which must be eliminated. Removal of the mean of the data over short time stretches (10-100 s) or high-pass filtering is typically used to reduce the effects of such drifts. Figure 10 demonstrates the impact of drifts on simulations for the Planck experiment, where the left map was produced without any filtering and the right map represents the same data but with a destriping algorithm applied. The scales of the maps are noticeably different and so is the visible pattern, which emphasizes the need for such filtering.

Other components in the data that must be removed are the effects of ground pickup from the 300-K Earth and changing atmospheric contributions during the scan. These signals are fixed to the reference frame of Earth and so are distinguishable from the celestial CMB signals. Even though any such data filtering removes some cosmological information, observing strategies are devised so that the filtering does not significantly compromise the sensitivity.

3.4.2 Reduction to maps.

The most intuitive representation of the CMB signal is a map on the sky. If done properly, this provides orders-of-magnitude compression of the data where no cosmological information is lost (for current typical experiments, the time streams have $N_t \sim 10^7$ samples this for 10 or more detectors whereas the number of sky pixels is $N_p \sim 10^5 - 10^6$).

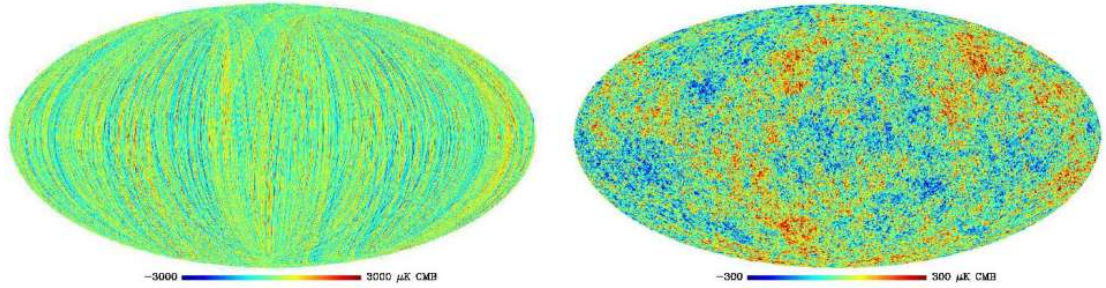


Figure 10: Effect of destriping on simulated sky maps. (Left) Map from a raw time stream. (Right) Map after applying a destriping algorithm (note the different scales). This simulation was done for the Planck High Frequency Instrument (38).

For an ideal time stream containing only the CMB signal on top of white noise, a map can easily be produced by averaging all observations that fall into a given pixel on the sky. This makes for a robust and fast algorithm, which scales linearly with the number of data samples. However, in a real experiment the filtering of the time streams introduces correlations that make this simple approach fail.

The optimal map estimate from the time stream is produced by maximizing the likelihood for the data given a certain noise model. The likelihood problem can be solved analytically, requiring the inverse of the covariance matrix in the time domain, as well as the calculation and inversion of the covariance matrix in pixel space. Whereas the time-stream covariance matrix is sparse, the covariances in the pixel domain have no special structure and the matrix inversion dominates the processing time, scaling with N_{pix}^3 . Parallelization of this procedure is possible. Iterative procedures are another approach and can reduce the required amount of computing power to scale as $N_{it}N_t \log N_t$, where N_{it} is the number of iterations. For those procedures, Monte Carlo methods are required to estimate the covariance, with a possible loss in sensitivity.

3.4.3 Power spectrum estimation.

Although the power spectrum could in principle be estimated directly from the time stream, it is more efficient to first produce a map and from it determine the power spectrum. The likelihood can then be expressed in the following form:

$$\mathcal{L} = \frac{1}{\sqrt{\det(C)}} \exp[-\mathbf{x}^T C^{-1} \mathbf{x}/2], \quad (10)$$

where \mathbf{x} represents the map vector and C the pixel-pixel covariance matrix in which the cosmological information is imbedded. The map contains contributions from both signal and receiver noise, and, similarly, the covariance matrix comprises signal added to noise. The likelihood is a measure of how well the scatter as seen in the data agrees with that expected from the combination of noise and the CMB signal. Maximizing the likelihood by setting $\frac{\delta \mathcal{L}}{\delta C_i} = 0$ leads to an equation that requires an iterative solution. A common and powerful method for likelihood estimations exploits a quadratic estimator, which uses for the error matrix an ensemble average (Fisher matrix) instead of the full curvature (see Reference 39 for details) and reaches convergence within only a few iterations. The maximum likelihood method offers an optimal evaluation of the power spectrum. However, its large matrix operations become impractical for upcoming experiments with fine-resolution maps of large fractions of the sky ($> 10^6$ pixels). Methods that exploit Monte Carlo simulations to approximate the analytical solution are thus an attractive option for the evaluation

Signal	$\Delta T_{cos}(nK)$	$\Delta T_{Gal}(nK)$	$\Delta T_{Lens}(nK)$	$\Delta T_{exp}(3\sigma)(nK)$	N_{wmap}^{opt}
lensing, $l = 1000$	300	150	-	35	1.5
$r = 0.1$ (SLS)	83	295	50	9.8	20
$r = 0.01$ (SLS)	26	295	50	3.1	200
$r = 0.1$ (reion)	54	780	-	6	50
$r = 0.01$ (reion)	17	780	-	1.9	500

Table 3: Required sensitivities to detect B-mode polarization signals Signal. For detecting the lensing signal at $l = 1000$ and the gravity wave at $r = 0.1$ and 0.01 , using either the surface of last scattering or the reionized plasma, we give the magnitude of the cosmological signal at its peak, the size of the galactic contamination, the magnitude of the lensing contaminant, the derived total experimental sensitivity to detect the signal (neglecting foregrounds) at 3σ , and the corresponding increase over that achieved with WMAP in 1 year. The foreground estimates are taken from the WMAP empirical full-sky relation, evaluated at 90 GHz at the appropriate l value. For small, selected patches of sky, foreground contamination will be significantly smaller, perhaps by an order of magnitude. Thus, the lensing signal should be observable from the ground with just eight WMAPs, for example, an array with eight times the number of detectors in WMAP, each with the same sensitivity, observing for one year and so on. The signatures of gravity waves from the surface of last scattering (SLS) should then also be detectable, even in the presence of foregrounds, although contamination from lensing and residual foreground levels will reduce sensitivity from what is shown in the table. Gravity wave signals from the reionized plasma have negligible contamination from lensing but, because of the needed full-sky coverage, larger foregrounds to deal with.

of the power spectrum and have become popular [e.g., the pseudo- C_l method (40)]. The use of Monte Carlo simulations for the evaluation of real data is a familiar concept to the high-energy physics physicist and is advantageous in that it enables a relatively easy treatment of various instrumental and processing artifacts or distortions.

3.4.4 Cosmological parameter estimation.

As described in Section 1, the development and contents of the Universe determine the characteristics of the CMB anisotropies and with that the shape of the CMB power spectrum. Current software tools such as *cmbfast* or *camb* calculate the expected power spectrum from a given set of cosmological parameters within a few seconds so that for a given measured power spectrum, the likelihood for different parameter values can be evaluated reasonably quickly. Still, the likelihood evaluation on a fine grid in the multidimensional parameter space requires huge computing resources so that the problem is typically approached via Markov chain Monte Carlo methods. A Markov chain begins with the evaluation of the likelihood at a specific point in the parameter space where its value in unences the next point for the likelihood evaluation. Repeating this leads to a sample density in parameter space proportional to the likelihood where projections onto one- or two-dimensional subspaces result in the marginalized likelihoods. By now, software packages such as *cosmomc* are available and in use by the CMB community.

4 FUTURE PROSPECTS

Here we discuss experiments needed to detect the B-mode signals of lensing at large l values and of gravity waves at intermediate and small l values. Table 3 shows the sensitivity required to make 3σ detections of several target signals. Estimates come from Equation 9, either for the full sky or for a smaller patch where the balance between sample variance and detector noise is optimized. We give expressions for the sensitivity to a feature in the power spectrum centered at l_0 and with width $\Delta l = l_0$ and for the fraction of the sky that accomplishes the balance: $(\Delta C_l/C_l)_{opt} \approx 3\Delta T_{exp}/\Delta T_{cos}$ and $f_{opt} \approx 1/2 \left(\frac{\Delta T_{cos}}{l_0 T_{exp}}\right)^2$. For our purposes, both the signal from lensing and from primordial gravity waves have approximately this shape. Here ΔT_{cos} is the (peak) cosmological signal of interest and ΔT_{exp} is the total sensitivity of the experiment, summing over all the observing time and all the detectors.

The lensing detection can be accomplished by observing for a year (from the ground at a good site such as the Atacama Desert in Chile or the South Pole) a patch of approximately 1.6 square degrees, with detectors having 1.5 times the WMAP sensitivity. The table also gives the sensitivities required to detect primordial B modes at various levels of $r = T/S$. Foregrounds will be a problem for $r \leq 0.01$, perhaps more so for the detection of the signal from the reionized plasma than from the surface of last scattering. A satellite experiment can detect the signal from the reionized plasma, where the lensing contamination is nearly negligible.

The Planck experiment (2007) has an order of magnitude in temperature sensitivity over WMAP. Polarization sensitivity was not a primary goal. Still, much has gone into making sure the residual systematic uncertainties (and foregrounds) can be understood sufficiently well to allow the extraction of polarization signals around 50 nK, corresponding to $r = 0.05$.

There is a program of experiments over the coming five to eight years. These will involve, progressively, tens, then hundreds, and finally a thousand or more detectors per experiment and will test polarization modulation schemes, effective scan strategies, foreground-removal methods, and algorithms for separating E and B modes.

Experiments with tens of detectors are already underway. The sister experiments QUaD and BICEP observe from the South Pole, using polarization-sensitive bolometers at 100 and 150 GHz. QUaD, with a 4-arcmin beam, is optimized for gravitational lensing, whereas BICEP, at approximately 40 arcmin, is searching for gravitational waves. MBI and its European analog BRAIN are testing the idea of using bolometers configured as an interferometer, and PAPPa is a balloon effort using waveguide-coupled bolometers from the Goddard Space Flight Center. These latter experiments have beams in the range of 0.5° to 1° .

Five initiatives at the level of hundreds of detectors have so far been put forth. Four use TES bolometers at 90, 150, and 220 GHz: CLOVER, the lone European effort, with an 8-arcmin beam; Polarbear, with a 4-arcmin beam; and EBEX and SPIDER, balloon-borne experiments with 8- and 20 70-arcmin beams, respectively (SPIDER and Polarbear will use antenna-coupled devices). The fifth uses coherent detectors at 44 and 90 GHz: QUIET, initially with a 12-arcmin beam, observing from the Atacama Desert. All are dedicated ground-up polarization experiments that build their own optical systems. The ACT and SPT groups, supported by the National Science Foundation, deploy very large telescopes to study both the cosmology of clusters via the SZ effect and fine-scale temperature anisotropies, and will likely propose follow-up polarimeters.

4.1 The Next Satellite Experiment

The reach of the next satellite experiment, termed CMBPOL as defined by the three-agency task force in the United States (36) and termed BPOL in Europe, is to detect the

signal from gravity waves limited only by astrophysical foregrounds. Examining Figure 6, we see that $r = 0.01$, and possibly lower values, can be reached. We should know a great deal from the suborbital experiments well before the 2018 target launch date. For studying polarization at large scales, where foregrounds pose their greatest challenge, information from WMAP and Planck will be the most valuable.

5 CONCLUDING REMARKS

There is considerable promise for new, important discoveries from the CMB, ones that can take us back to when the Universe's temperature was between the Grand Unified Theory and Planck energy scales. This is particle physics, and while we hope accelerators will provide crucial evidence for, for example, the particle nature of dark matter, exploring these scales seems out of their reach.

In some ways, cosmology has followed the path of particle physics: It has its Standard Model, accounting for all confirmed phenomena. With no compelling theory, parameter values are not of crucial interest. We cannot predict the mass of the top quark, nor can we predict the primordial energy densities. Each discipline is checking consistency, as any discrepancies would be a hint of new physics.

The CMB field is not as mature as particle physics. It needs considerable detector development, even for current experiments. There is rapid progress, and overall sensitivity continues to increase. Foregrounds are certainly not sufficiently known or characterized. There is a great deal of competition in the CMB, like the early days of particle physics before the experiments grew so large that more than one or two teams exploring the same topic worldwide was too costly. For the moment, this is good, as each team brings something unique in terms of control of systematics, frequencies, regions of the sky scanned, and detection technology. However, there is a difference in the way results are reported in the two fields. In the CMB field, typically almost nothing is said about an experiment between when it is funded and when it publishes. Here publishing means that results are announced, multiple papers are submitted and circulated, and often there is a full data release, including not only of raw data and intermediate data products but sometimes support for others to repeat or extend the analyses. The positives of this tradition are obvious. However, one negative is that one does not learn the problems an experiment is facing in a timely manner. There is a degree of secrecy among CMB scientists.

There are other differences. CMB teams frequently engage theorists to perform the final analysis that yields the cosmological significance of the data. Sophisticated analysis techniques are being developed by a set of scientists and their students who do not work with detectors but do generate a growing literature. There are as yet no standardized analysis techniques; effectively each new experiment invents its own. The days appear to be over where the group of scientists that design, build, and operate an experiment can, by themselves, do the full scientific analysis. Another distinction is that there is no one body looking over the field or advising the funding agencies, and private funds sometimes have a major impact. Nearly all CMB scientists are working on multiple projects, sometimes as many as four or five, holding that many grants. More time is spent writing proposals and reports and arranging support for junior scientists, for whom there is little funding outside of project funds. This is certainly not the optimum way to fund such an exciting and promising field.

6 ACKNOWLEDGMENTS

The authors have enjoyed many productive conversations with colleagues at their institutions in the course of preparing this review. The authors are particularly grateful for helpful comments from Norman Jarosik, Bernd Klein, Laura La Porta, and Kendrick Smith. We also wish to acknowledge our collaborators in QUIET and CAPMAP for frequent discussions of relevant issues. This work was partially supported by grants from the National Science Foundation: PHY-0355328, PHY- 0551142, and ASTR/AST-0506648.

References

1. Kamionkowski M, Kosowsky A. *Annu. Rev. Nucl. Part. Sci.* 49:77 (1999)
2. Dodelson S. *Modern Cosmology*. Acad. Press (2003)
3. Penzias AA, Wilson RW. *Astrophys. J.* 142:419 (1965)
4. Partridge RB. *3K: The Cosmic Microwave Background Radiation*. Cambridge, NY: Cambridge Univ. Press (1995)
5. Fixsen DJ, et al. *Astrophys. J.* 483:586 (1996)
6. Feng JL, Rajaraman A, Takayama F. *Phys. Rev. D* 68:063504 (2003)
7. Smoot GF, et al. *Astrophys. J.* 396:1 (1992)
8. Hinshaw G, et al. *Astrophys. J.* In press (2007)
9. Bock J, et al. *astro-ph/0604101* (2006)
10. Smith TL, Kamionkowski M, Cooray A. *Phys. Rev. D* 73(2):023504 (2006)
11. Spergel DN, et al. *Astrophys. J.* In press (2007)
12. Page L, et al. *Astrophys. J. Suppl.* 148:233 (2003)
13. Readhead ACS, et al. *Science* 306:836 (2004)
14. MacTavish CJ, et al. *Astrophys. J.* 647:799 (2006)
15. Tegmark M, et al. *Phys. Rev. D* 69:103501 (2004)
16. Hu W, Sugiyama N. *Phys. Rev. D* 51:2599 (1995)
17. Eisenstein DJ, et al. *Astrophys. J.* 633:560 (2005)
18. Bennett CL, et al. *Astrophys. J. Suppl.* 148:97 (2003)
19. Page L, et al. *Astrophys. J.* In press (2007)
20. La Porta L, Burigana C, Reich W, Reich P. *Astron. Astrophys.* 455(2):L9 (2006)
21. Carretti E, Bernardi G, Cortiglioni S. *MNRAS* 373:93 (2006)
22. Hanany S, Rosenkranz P. *New Astron. Rev.* 47(11 12):1159 (2003)
23. Pietranera L, et al. *MNRAS*. In press (2007)
24. Finkbeiner DP, Davis M, Schlegel DJ. *Astrophys. J.* 524:867 (1999)

25. Vaillancourt JE. Eur. Astron. Soc. Publ. Ser. 23:147 (2007)
26. Benoit A, et al. Astron. Astrophys. 424:571 (2004)
27. Ponthieu N, et al. Astron. Astrophys. 444:327 (2005)
28. Huffenberger KM, Eriksen HK, Hansen FK. Astrophys. J. 651:81 (2006)
29. Stivoli F, Baccigalupi C, Maino D, Stompor R. MNRAS 372:615 (2006)
30. Verde L, Peiris HV, Jimenez R. J. Cosmol. Astropart. Phys. 1:19 (2006)
31. Barkats D, et al. Astrophys. J. Suppl. 159(1):1 (2005)
32. Ryle M. Proc. R. Soc. A 211:351 (1952)
33. Zmuidzinas J. Appl. Optics 42:4989 (2003)
34. Mather JC. Appl. Optics 21:1125 (1982)
35. Tegmark M. Phys. Rev. D 56:4514 (1997)
36. Smith K. New Astron. Rev. 50(11 12):1025 (2006)
37. Crawford T. astro-ph/0702608 (2007)
38. Couchout F, et al. CMB and physics of the early universe. <http://pos.sissa.it/cgi-bin/reader/conf.cgi?confid=27> (2006)
39. Bond JR, Jaffe AH, Knox L. Astrophys. J. 533:19 (2000)
40. Hivon E, et al. Astrophys. J. 567:2 (2002)